

ABSTRACT

Title of Thesis:

**THERMO-MECHANICAL ANALYSIS OF
ENCAPSULATED BALL-WEDGE WIRE
BONDS IN MICROELECTRONICS, USING
RALEIGH-RITZ MODELING**

Krishna Kumar Jinka, Master of Science, 2006

Thesis directed By:

Professor Abhijit Dasgupta

Department of Mechanical Engineering

This study addresses encapsulated wire bonds in chip-on-board (CoB) multi chip modules, which provide a low cost option for dealing with the current trend towards compact microelectronic packages with increased I/O, higher reliability and lower cost. The focus is on thermomechanical stresses caused in the bond wires when the encapsulant is cooled from high curing temperatures and subsequently subjected to thermal cycling loading. The stresses generated in bond wires due to thermal expansion mismatches, in an encapsulated CoB are very complex and are driven by both global and local thermal expansion mismatches between: (i) glob-top encapsulant and the silicon die, (ii) encapsulant and the wire, and (iii) encapsulant and the substrate assembly.

A 2D stress analysis model based on the variational Raleigh-Ritz (RR) method is developed, to estimate thermomechanical stresses in the bond wire, based on elastic analysis. The study focuses on detailed parametric investigation of different encapsulated CoB configurations. The initial wire profile, before encapsulation, is first modeled with RR 2-D trial functions based on cubic splines. This predicted geometry is then used for the subsequent thermomechanical stress analysis after encapsulation, based on trial functions composed of polynomials and exponential functions. The results are calibrated with Finite Element Analysis. Plastic deformations are ignored in the current analysis, as a first-order approximation. This model is therefore suitable for parametric design sensitivity studies and qualitative ranking of design options, but not for quantitative predictions of thermal cycling durability. The results show that the region above the ball bond is the predominant failure site. The RR 2-D model has a well-defined range of validity for CoB Ball-Wedge wire bond configurations with stiff encapsulants ($E \geq 3$ GPa) and thin wires (dia ≤ 2 mils). Also, the trend of maximum elastic strains obtained from the RR 2-D model is found to be in qualitative agreement with thermal cycling fatigue test data obtained from the literature.

THERMO-MECHANICAL ANALYSIS OF ENCAPSULATED BALL-WEDGE
WIRE BONDS IN MICROELECTRONICS, USING RALEIGH-RITZ MODELING

By

Krishna Kumar Jinka

Thesis submitted to the Faculty of the Graduate School of the
University of Maryland, College Park, in partial fulfillment
of the requirements for the degree of
Master of Science
2006

Advisory Committee:
Professor Abhijit Dasgupta, Chair
Associate Professor F. Patrick McCluskey
Professor Bongtae Han

© Copyright by
Krishna Kumar Jinka
2006

DEDICATION

To my
Parents and friends

ACKNOWLEDGEMENTS

First and foremost, I am very grateful to my advisor and mentor Dr. Abhijit Dasgupta, who has relentlessly encouraged and helped me refine my engineering research skills. His profound knowledge combined with his very amiable nature has been inspiring and immensely helpful.

My special thanks to Dr. Sanka Ganesan, who was the Principal Investigator of my research. He has provided me encouragement and support through out the course of my research.

I thank my committee members Dr. F. Patrick McCluskey and Dr. Bongtae Han, for their cooperation and valuable suggestions, and extend my sincere gratitude for being on my committee.

I am grateful to Dr. Sharon Ling from Applied Physics Laboratory for funding this study and for technical collaborations.

I would also like to thank the members of the CALCE Electronic Products and Systems Center for providing technical resources to conduct my research and particularly Dr. Keith Rogers for his help with various equipments in the laboratory and guidance in failure analysis.

I would like to express my gratitude to Dr. Karumbu Meyyappan, for his technical help with implementation of cubic splines for ball-wedge wire profiles. Navigating my way through the MS program was made easier and more enjoyable through my friendship with my colleagues including but not limited to Leila Jannesari, Krista Soderholm, Joseph Varghese, Dan Farley, Zhou Yuxun, Gayatri Cuddalorepatta and Shaughn Roettele.

I take this opportunity to thank my best friend Swathi Lakkarsu, for all the encouragement, assistance and backing she gave me through out the course of my research and study.

Most of all, I specially wish to thank my dear parents, with out whom I wouldn't be what I am today. I don't have enough words to express my earnest gratitude to them for being the driving force behind me all through these years and providing me with able support and comfort when I needed them most.

TABLE OF CONTENTS

DEDICATION.....	ii
ACKNOWLEDGEMENTS	iii
TABLE OF CONTENTS	v
LIST OF FIGURES	vi
LIST OF TABLES	viii
1 Introduction.....	1
1.1 Background and Problem Statement.....	1
1.2 Wirebonding in Microelectronics	5
1.3 Wire Material	7
1.4 Ball Bonding of Gold Wires	8
1.5 Failure Mechanisms	10
1.6 Virtual Qualification	12
1.7 Scope of the Current Thesis.....	14
1.8 Nomenclature and Terminology Used.....	16
2 Optimal Ball-Wedge Wire Profile in Unencapsulated Chips	19
2.1 Ball-Wedge vs. Wedge-Wedge Optimal Profiles	19
2.2 Approach.....	20
2.2.1 Model	21
2.2.2 Determination of Wire Profile	23
3 Prediction of Thermo-Mechanical Stresses in Encapsulated CoB Bond Wire	27
3.1 Development of the Model Guided by 2D Finite Element Analysis (FEA)	27
4 Results and Discussion.....	39
4.1 Determination of Wire Profile and Loop Height in Unencapsulated Ball-Wedge Wire-Bonds.....	39
4.2 Comparison of the RR model with FEA for Thermomechanical Analysis of Encapsulated Ball-Wedge Wire-Bond	43
4.3 Parametric Studies	44
4.4 Comparison of Test Results [APL, 2005] with Model Predictions	50
5 Conclusions, Contributions and Suggestions for Future Work	53
5.1 Conclusions.....	53
5.2 Contributions.....	54
5.3 Limitations of the Existing Model	55
5.4 Suggestions for Future Work	56
Appendix A	58
Appendix B	64
Appendix C	67
Appendix D.....	73
References.....	89

LIST OF FIGURES

Figure 1.1 Ball-wedge wire bond.....	2
Figure 1.2 Shaped ball-wedge wire bonds.....	3
Figure 1.3 Critical failure sites in a typical CoB	4
Figure 1.4 (a) Ball bond; (b) Wedge bond [Chandrasekaran, A., 2004].....	6
Figure 1.5 Bonding mechanism [Harman, 1997].....	9
Figure 1.6 Bonding tool.....	9
Figure 1.7 IC Failures [Meyyappan, 2004].....	10
Figure 1.8 Schematic of a typical encapsulated chip.....	15
Figure 2.1 (a) Ball-wedge profile (b) Wedge-wedge profile	20
Figure 2.2 Labels used for the derivation of strain in a curved beam.....	23
Figure 2.3 Schematic of wire bonded CoB.....	23
Figure 2.4 Calculated wire profile based strain energy minimization	24
Figure 3.1 Schematic of encapsulated ball-wedge model geometry.....	29
Figure 3.2 FEA model with meshed elements.....	29
Figure 3.3 Contour plots of displacements in the encapsulant obtained from FEA in (a) x-direction and (b) y-direction.....	30
Figure 3.4 Modeling domains in the encapsulant	30
Figure 3.5 Displacement profiles in the encapsulant in the x-direction from (a) FEA and (b) the RR model.....	32
Figure 3.6 Displacement profiles in the encapsulant in the y-direction from (a) FEA and (b) the RR model.....	33
Figure 4.1 Determination of optimal wire profile.....	40
Figure 4.2 Loop height vs. span for minimum strain energy wire profiles	41
Figure 4.3 Wire profiles for (a) various spans ($H=25$ mils) and (b) various offsets ($D=40$ mils).....	41
Figure 4.4 Parametric analysis for various spans ($H=25$ mils).....	42
Figure 4.5 Parametric analysis for various height offsets ($D=40$ mils).....	42
Figure 4.6 Comparison of (a) axial and (b) bending elastic strains in FEA and the RR model.....	44
Figure 4.7 Comparison of total elastic strains between FEA and the RR model.....	44
Figure 4.8 Comparison of maximum elastic strain between FEA and the RR model	46
Figure 4.9 Variation of % difference between the FEA and the RR model (in max. elastic strain) with Young's Modulus of Encapsulant.....	47
Figure 4.10 Contour plot of elastic strain for change in die height (H) and span (D)	47
Figure 4.11 Contour plot of elastic strain for change in CTE and Young's Modulus of the encapsulant.....	48
Figure 4.12 Axial strain along the span predicted by (a) FEA and (b) the RR model for CoBs with different encapsulant Young's Modulus	49
Figure 4.13 Variation of % difference between FEA and the RR model (in max. elastic strain) with diameter of the bond wire.....	49
Figure 4.14 Comparison of the fatigue test results [APL, 2005] with (a)the RR model and (b) FEA.....	51
Figure 5.1 Ball-Wedge wire profile under thermal loading.....	56
Figure A 1 Schematic of Encapsulated CoB Configuration.....	58

Figure A 2 Schematic of the Deformed CoB showing displacement in x-direction ..	59
Figure A 3 Schematic of the Deformed CoB showing displacement in y-direction ..	62
Figure C 1 Plot of Strain Energy vs. A	68
Figure C 2 Plot of Strain Energy vs. B	69
Figure C 3 Plot of Strain Energy vs. C	69
Figure C 4 Plot of Strain Energy vs. u_{2sub}	70
Figure C 5 Plot of Strain Energy vs. u_{die}	70
Figure C 6 Plot of Strain Energy vs. v_{die}	71
Figure C 7 Plot of Strain Energy vs. $v_{dieattach}$	71
Figure C 8 Plot of Strain Energy vs. K	72
Figure C 9 Plot of Strain Energy vs. G	72

LIST OF TABLES

Table 1.1 Three wirebonding processes.....	6
Table 4.1 Design Parameters to compare the RR model with FEA.....	43
Table 4.2 Parametric variations used to validate RR model.....	45
Table 4.3 Thermal cycling test results [APL, 2005].....	50

1 Introduction

The current trend in electronic packaging is to develop compact packages with increased I/O, higher reliability and lower cost. There are several packaging methods which can accommodate the increased density and complexity of today's modern systems while providing the high electrical and thermal performance necessary for advanced integrated circuits like multi-chip modules (MCMs) for high density packaging. Wire bonded chip-on-board (CoB) multi chip modules provide a low cost option for many electronic products. The process of wire bonding starts with attaching the back of a bare chip directly to the PCB with either conductive or non-conductive epoxy or solder die attach materials. This process is followed by thermocompression bonding of gold wire to bond pads and PCB.

1.1 Background and Problem Statement

Low-temperature electronics technology is of great interest for space exploration missions. These include missions to planets in the solar system, earth-orbiting deep-space probes, and remote sensing and communication satellites, where application temperatures can be as low as -125°K . The knowledge gained from these special applications will also greatly benefit terrestrial applications. For example, improvements in electrical performance of electronic devices due to increased carrier mobility, decreased interconnect resistance, and reduced noise under low temperature environments, can enable high performance microprocessors. Even with these interests and advancements, there is very little effort in understanding and advancing the capabilities and reliability of electronic packaging and interconnects at low temperatures, and under large cyclic

temperature ranges that take electronics down to low temperatures. One of the biggest challenges is that material properties at -125°K are not well characterized. In the COB context, the important material properties at low temperature are those of the encapsulant material and the die attach material. These materials may become excessively stiff at low temperatures and exert high stresses on wire bonds.

Chip-On-Board technology involves attaching a semiconductor die to a substrate and the interconnection between the die and the substrate is accomplished through wire bonding. Wire bonding selected for this application is the ball-wedge configuration. Ball bonding is achieved on the semiconductor die pad and wedge bonding on the substrate pad. Usually thermosonic wire bonding is carried out at around 175°C . Initial experiments with this configuration showed that there were wire failures during exposure to low temperature.

Figure 1.1 shows a ball-wedge bonded wire in typical unencapsulated CoB assembly [Kulicke & Soffa, 2001]. These CoBs typically contain a silicon die, substrate, die attach material, encapsulant and wire bonds. The die is attached to the substrate using die attach material. The attachment material serves mechanical, electrical, and thermal functions. [Pecht, 1991]

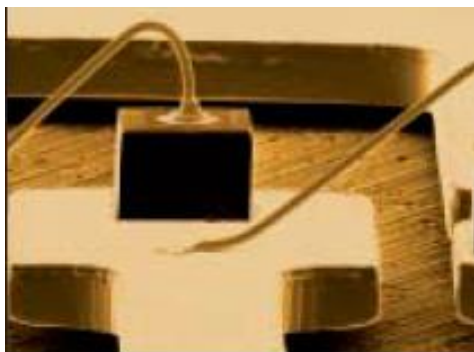


Figure 1.1 Ball-wedge wire bond

However, in high density interconnect packages, the ball-wedge bonded wire profile is shaped to achieve a low loop to provide clearance and to avoid interference from adjacent wires [Chylak et al., 2006]. Figure 1.2 shows a CoB with shaped ball-wedge wire bonds. The shaping is done by adjusting the control parameters of the bonding tool during the bonding process.

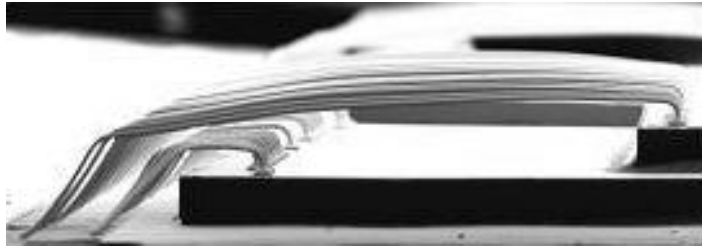


Figure 1.2 Shaped ball-wedge wire bonds

The environmental and operational loads place severe thermo-mechanical stresses on these devices. One of the critical phases in the design is to identify the design weaknesses and dominant failure mechanisms associated with the application. Some of the critical failure sites (Figure 1.3) identified in such a CoB assembly are

1. Failure of bond wires at the wedge bond
2. Failure of bond wires at the wedge bond heel
3. Failure of bond wires near the peak
4. Failure of bond wires above the ball bond
5. Failure of bond wires at the ball bond pad

The coefficient of thermal expansion mismatch between the different layers coupled with the thermal cycling environment can also cause weakening of the die attach material and cracking of the silicon die. However, the predominant failure site observed in these CoBs is the fatigue failure of the bond wires. Also, accelerated thermal cycling of test samples revealed wire bond failures as the dominant failure mechanism.

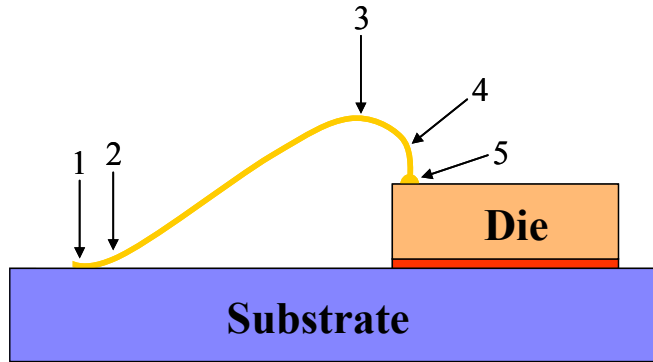


Figure 1.3 Critical failure sites in a typical CoB

Effective stress analysis and fatigue analysis methods are essential for proper design and reliability assessment for the wirebonded interconnects. In order to investigate the failure induced due to thermal cycling loading, a quick and efficient stress analysis scheme is essential. The life-cycle stresses in the wire bond are dominated by those imposed by the CoB encapsulant. We see the investigation of this stress as a two-step process because of the fabrication steps. In step 1, the wire is bonded in the absence of any encapsulant and this geometry forms the initial condition for the subsequent encapsulation process. In step 2, the encapsulation process applies thermo-mechanical forces to this geometry and all subsequent temperature cycling simulation adds to these stresses. In our approach, we are addressing each of these two steps separately.

In step 1, we make simplified predictions of the wire profile based on minimization of the elastic bending strain energy. The analysis is suitable for simple parametric studies and for making relative comparisons between different profiles for design tradeoffs. We do not attempt to predict the absolute stress or strain or durability, which would require plastic analysis.

The wire stress induced by thermal expansions in an encapsulated CoB is very complex, and is driven by both global and local thermal expansion mismatches between

(i) glob-top encapsulant and the silicon die, (ii) encapsulant and the wire, and (iii) encapsulant and the substrate assembly. In step 2, a 2D stress analysis model based on Raleigh-Ritz (RR) method is developed to predict stresses based on elastic analysis only. The RR method is chosen, as it is one of the popular energy-based modeling techniques. Because of the elastic idealization, the second step is suitable only for parametric investigation and comparison of encapsulated bond wire stresses in different CoB configurations. This study can serve as the starting point for subsequent elastic-plastic analyses in future, for detailed stress, strain and durability estimates.

The goal of this study is to develop quantitative semi-analytic models that can help to estimate the optimal wire profile geometry in wire bonded Chip-On-Board (CoB) technology, shown in Figure 1.3, and to estimate the subsequent thermo-mechanical stress in the ball-wedge bond wire, after encapsulation. The intent is to develop an elastic model that can be used to conduct design trade-off analyses using parametric sensitivity studies for different CoB configurations.

1.2 Wirebonding in Microelectronics

The microelectronics industry widely uses wire bonding as a means of interconnecting bond pads on the die to the bond pads on a substrate using thin wire and a combination of heat pressure and/or ultrasonic energy.

Wire bonding continues to be the dominant interconnection technology in industry. In 1996 it was estimated that about 4×10^{12} wires were bonded per year. [Harman, 1997]. There are two basic forms of wire bonds, namely ball bond and wedge bond, as shown in Figure 1.4. Approximately 93% of all semiconductor packages are manufactured using ball bonding method, while wedge bonding is used to produce about

5% of all assembled packages [<http://extra.ivf.se/ngl/documents/ChapterA/chapterA.pdf>]. Ball bonding allows smaller bond pads, smaller pitch and hence a very high I/O. This is very desirable in the semiconductor industry.

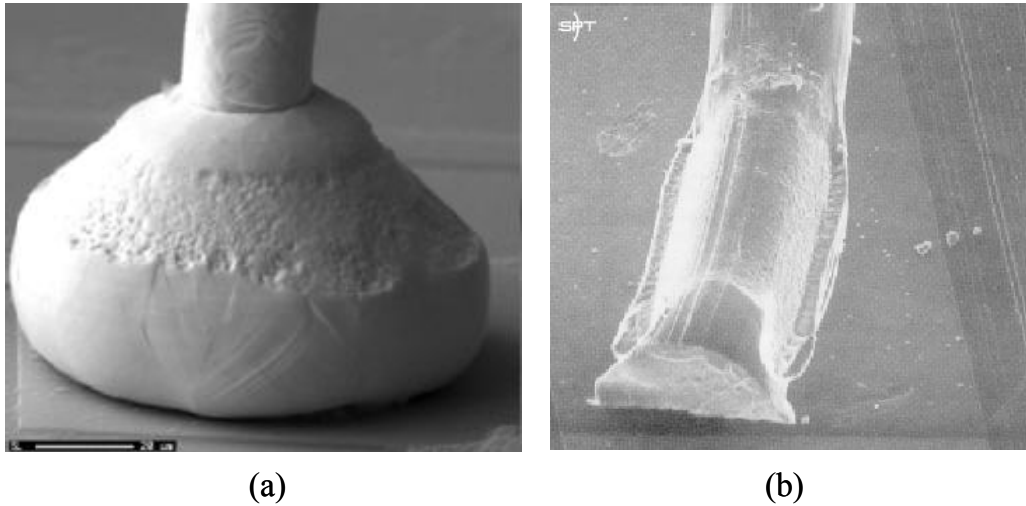


Figure 1.4 (a) Ball bond; (b) Wedge bond [Chandrasekaran, A., 2004]

Depending on the bonding agent (heat and ultrasonic energy), the bonding process can be categorized into three major processes: thermocompression bonding (T/C), ultrasonic bonding (U/S), and thermosonic bonding (T/S), as shown in Table 1.1.

Table 1.1 Three wirebonding processes

Wirebonding	Pressure	Temperature	Ultrasonic energy	Wire	Pad
Thermocompression	High	300-500 °C	No	Au,	Al, Au
Ultrasonic	Low	25 °C	Yes	Au, Al	Al, Au
Thermosonic	Low	100-150 °C	Yes	Au	Al, Au

Gold and aluminum are the usual wire materials, although copper and silver have also been used. Gold is mostly used in small signal devices because of its ability to be

drawn into small-diameter wires (1 mil) and to create non-directional thermocompression ball bonds. Ultrasonically bonded aluminum wire, which is less expensive, is mostly used in power devices, where thicker wires are needed and where a monometallic bond is preferred for its immunity to the formation of intermetallics [Pecht, 1999]. Gold wire can be bonded in the shape of a wedge or a ball. Ball bonds can be used in very tight spacing. Aluminum wire can only be wedge bonded and so is limited when spacing is tight.

Ultrasonic (Wedge-Wedge) bonding is done at room temperature with the application of ultrasonic energy. This is in contrast to the technologies used widely for gold wire bonding. Thermo-compression, used in Ball-Stitch bonding is done at a very high temperature with the application of heat. Thermosonic, also used in Ball-Stitch bonding, is done at around 100-150°C along with the ultrasonic energy.

Henceforth, the discussions would be limited to ball-wedge bonded gold wires.

1.3 Wire Material

Gold wire is used extensively for thermocompression bonding, although either thermocompression or thermosonic bonding can be used with gold. In producing gold bonding wires, control of the surface finish and surface cleanliness are of the greatest importance in ensuring the formation of a strong bond and preventing the clogging of bonding capillaries. Pure gold can usually be drawn to an adequate breaking strength (the ultimate tensile strength of the wire) and proper elongation (the ratio of the increase in wire length at rupture to the initial wire length, given as a percent). Ultra-pure gold is very soft, and even after the addition of small amounts of impurities such as 5 to 10 ppm by weight of beryllium or 30 to 100 ppm by weight of copper, the gold is still ductile.

Beryllium-doped wire is stronger than copper-doped wire by about 10-20% under most conditions. The increased strength of the Be-doped wire is advantageous for automated thermocompression bonding, where high-speed capillary movements generate higher stresses than in manual bonders [Pecht, 1999]. Gold wires for ball bonding are supplied in the annealed condition [Harman, 1997].

1.4 Ball Bonding of Gold Wires

A simplified procedure for making a ball-stitch wire interconnection with a capillary tool is shown in Figure 1.5. (1) Gold wire is fed through the capillary and an Electronic Flame Off (EFO) spark melts the wire. A gold ball forms at the end of the wire. (The ball typically consumes about 500 μm of a 25- μm diameter wire, but is less for fine-pitch bonding.) (2) The wire is retracted so that the ball is positioned against the bottom of the capillary. (3) The tool is lowered to the bond pad, and the Au ball is pressed against it. The interface rises to the bonding temperature (from the heated work holder), ultrasonic energy is applied, and the ball bond is formed. (4) The tool is raised, leaving the ball welded to the surface, and forming the wire loop as it moves toward the second bond position. (5) The bond pad is positioned beneath the bonding tool (or capillary). (6) The tool is lowered, as in (3), to make a bond. This bond, and any subsequent bonds made before the wire is broken off, is called a stitch bond. Sometimes the final bond is called the crescent bond because of its shape. (7) After the stitch bond is made, the capillary tool is raised, and a wire clamp above the capillary tool pulls and breaks the wire free. The tool rises up, the clamp lowers the wire sufficiently to allow another ball to be made, and the bonder is ready to repeat the bonding cycle. [Harman, 1997]

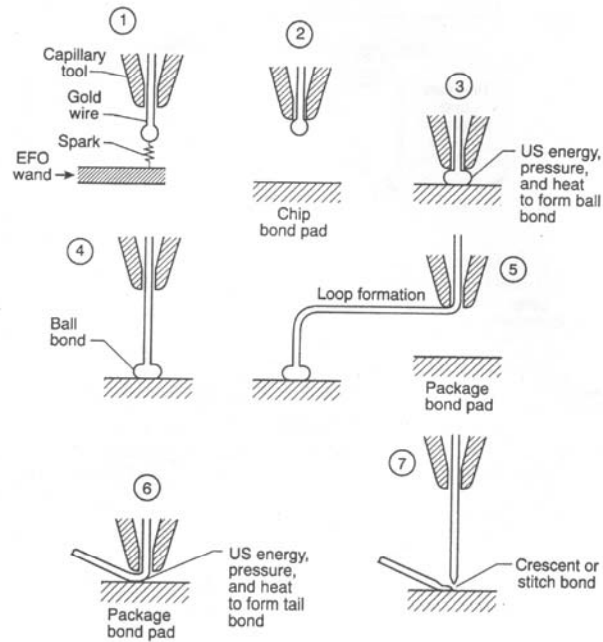


Figure 1.5 Bonding mechanism [Harman, 1997]

The illustration in Figure 1.5 helps us better understand the bonding mechanism, which is important in studying the durability of ball bonded wires. A typical ball bonding tool used in this operation is shown in Figure 1.6.

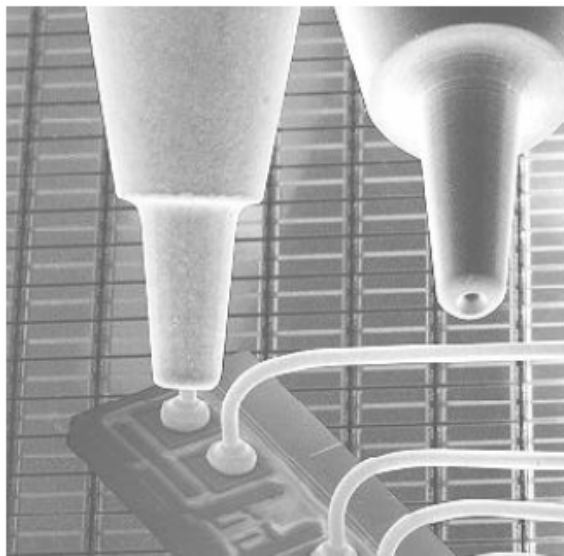


Figure 1.6 Bonding tool

1.5 Failure Mechanisms

Wire bond failure is the most common source of failure in an IC in spite of its universal use and high volume of wire bonding. Wire bonding failures account for almost 26% of all IC failures. Figure 1.7 shows different failure types.

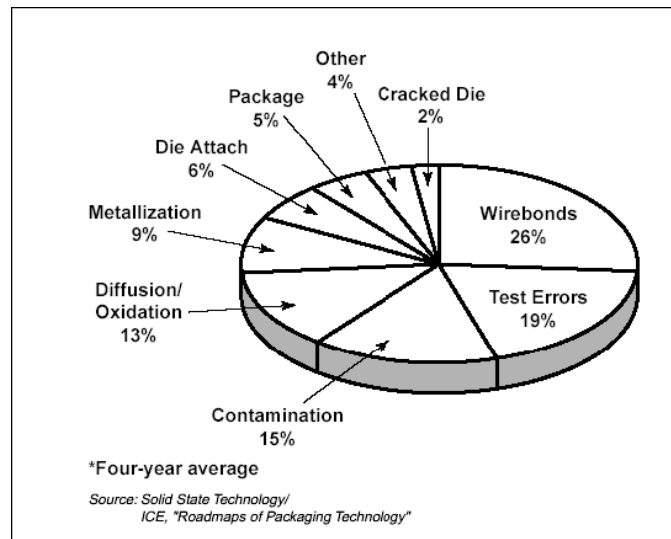


Figure 1.7 IC Failures [Meyyappan, 2004]

A variety of different thermal cycle failures have been observed in plastic-encapsulated packages, often where failure occurs above the neck of the Au ball.

Several failure mechanisms have been identified and classified, and damage models have been proposed [Dasgupta, Pecht 1991]. Pecht et al., [1994] described the failures that occur in wire bonded plastic encapsulated microelectronics (PEM). These failure mechanisms include, but are not limited, to die fracture, corrosion, metallization deformation, wire sweep, cratering of wirebond pad, wirebond fracture and liftoff, delamination, substrate cracking and electrical leakage.

Corrosion in wirebond, bondpad and leadframe is caused by several factors like ionic contaminants, encapsulant material, temperature and metal composition resulting in

a range of problems from change in thermal properties to loss in strength. Pecht [Pecht, 1990] provides a foundation to which prior and future corrosion models can be compared.

The wire can break at the heel of a wedge bond due to the reduced cross-section of the wire. Cracks in the heel of a ball bond can arise as a result of excessive flexing of the wire during loop formation, especially when the level of the second bond is significantly lower than the first; repeated flexing and pulling of the wire occurs as the device heats and cools during temperature cycling, due to thermal mismatches [Harman 1974]. Meyyappan et al., developed a wire fatigue model to predict failure due to flexure in wedge-wedge bonded power electronic modules before encapsulation at CALCE Electronic Products and Systems Center [Meyyappan, 2004]. Pang et al., used a 2D nonlinear finite element analysis to study the effect of encapsulant material properties on the ball-wedge bond wire stress under thermal loading between -40°C and 125°C , and to predict fatigue failure life [Pang et al., 1997].

Thermal cycling can cause wires to lift-off due to shear stresses generated between the bond pad-wire interface and between bond pad-substrate interfaces. This can be reduced if the coefficient of thermal expansion (CTE) mismatch between the materials at the interface is reduced. Ramminger [Ramminger et al., 2003] developed physics-of-failure based models to study wire lift-off failures. Hu [Hu et al., 1991], proposed a probabilistic approach for predicting thermal fatigue life of wire bonding in microelectronics. Chidambaram [Chidambaram, 1991] used a 3D nonlinear finite element analysis and test data to study the effect of encapsulant on ball bond stresses under thermal loading, and developed a numerical procedure to simulate reliability testing results.

During thermal cycling, the wires are subjected to flexure in response to the rise in temperature. The flexing motion results in stress reversals in the bond wire, causing cracks to appear at the ball bond, near the wire loop peak and near the wedge bond heel. In open cavity packages cracks in the bond wire can arise due to a sharp-heeled bonding tool, bonding machine vibration, and by operator motion or due to the wire loop formation. It is very important to design and produce an optimum loop profile since a sub optimal loop profile can result in unnecessary flexing of the wire. Also, an asymmetrically bonded wire (wires bonded with a height offset) promotes cracking more than a wire bonded without any height offset [Harman, 1997]. A variety of different thermal cycle failures have been observed in plastic-encapsulated devices, often where failure occurs above the neck of the Au ball. This failure results from the difference in thermal expansion between the wire, the Si and the plastic [Harman, 1997].

Thermal cycling experiments have been reported in the literature, on encapsulated CoBs with ball bonded Au wires [APL, 2005]. Among all the test vehicles that failed, the majority of failures occurred at the neck of the ball bond, and a few at the peak of the wire loop and at the heel of the wedge bond. Hence, in the current study, it was decided to focus on the stresses that drive the failures at the ball bond.

1.6 Virtual Qualification

The criteria for wire bonding evaluation vary, depending on the application requirements. The visual method of inspection uses an optical microscope, scanning electron microscope (SEM) and other analytical instruments to find the defective bonds nondestructively. Mechanical testing, often involving destructive methods, is used to

evaluate the strength of the bonds. Evaluation methods can be found in several published standards, but the most common standard is MIL-STD-883. They include:

- Internal visual (Method 2010; Test condition A and B)
- Delay measurements (Method 3003)
- Destructive bond pull test (Method 2011)
- Nondestructive bond pull test (Method 2023)
- Ball bond shear test
- Temperature cycling test (Method 0101, Test Condition C)
- Constant acceleration (Method 2001; Test condition E)
- Random vibration (Method 2026)
- Mechanical shock (Method 2002)
- Stabilization bake (Method 1008)
- Moisture resistance (Method 1004)

Temperature cycling tests subject the wire bond interconnects to cyclic stresses. The failure mechanisms addressed by the temperature cycling test include fatigue failures due to wire flexure at the ball bond, at the wedge bond heel, and due to shear stresses at the bond pad-substrate interface, and at the wire-substrate interface.

This study focuses primarily on the stress that induces failures of ball-wedge bonded wires commonly seen in encapsulated CoBs. The approach explained in this study to estimate the stress is generic and can be extended to any semiconductor device with encapsulated ball-wedge bonded wire interconnections.

A typical CoB test vehicle for Mar's mission has been required to sustain 1500 accelerated thermal cycles between -125°C and $+85^{\circ}\text{C}$ in order to be qualified for use.

This procedure is meant to detect modules that are likely to fail by cyclic fatigue in operational life when the assembly is subjected to cyclic strain as a result of thermal cycling or power cycling.

While this traditional procedure is well accepted, it has two major shortcomings. The procedure is costly and time consuming and is therefore undesirable in today's product development environment of shortened design cycles and quick time-to-market. It is no longer acceptable to make a prototype, subject it to a series of standardized tests, analyze the failures, fix the design, and test again. Instead, a fundamental model is needed to assess the susceptibility of CoB designs to wire stress fatigue without conducting such extensive qualification tests. Such a model should be based on a fundamental understanding of the thermo-mechanical mechanism that causes wire stress failure in electronic systems. The use of such models to qualify assemblies for field use is known as virtual qualification.

1.7 Scope of the Current Thesis

Focus of this study is limited to developing semi-analytic elastic models that can provide ranking of design options through parametric sensitivity studies. Such a model should be capable of predicting the wire profile before encapsulation and thermomechanical stresses induced in wedge-ball wire interconnections due to temperature changes after plastic encapsulation. The model is energy-based since every physical system would prefer to take up a configuration where it would store minimum potential energy. Identifying the most stable configuration can help decide the best loop profile and improve the accuracy of stress prediction in encapsulated ball bonded wires.

These models can eventually facilitate virtual qualification of ball-wedge wire bonds, if they can be extended to include plastic deformations.

Chapter 2 describes the 2D elastic Raleigh-Ritz (RR) model which determines the minimum-energy ball-wedge wire loop profile in unencapsulated CoB configurations, for a given set of design inputs.

Chapter 3 describes the 2D elastic Raleigh-Ritz (RR) model which estimates the thermomechanical stresses in encapsulated ball-wedge wires in CoB.

The determination of optimal wire profile and loop height, validation of the stress predicted by semi analytical model, sensitivity analysis and model limitations are explained in Chapter 4.

The thesis is concluded in Chapter 5 with the list of contributions and suggestions for future work.

Figure 1.8 shows the schematic of a cross sectional view of a typical encapsulated chip with some of the commonly used terminology seen throughout the text of the report.

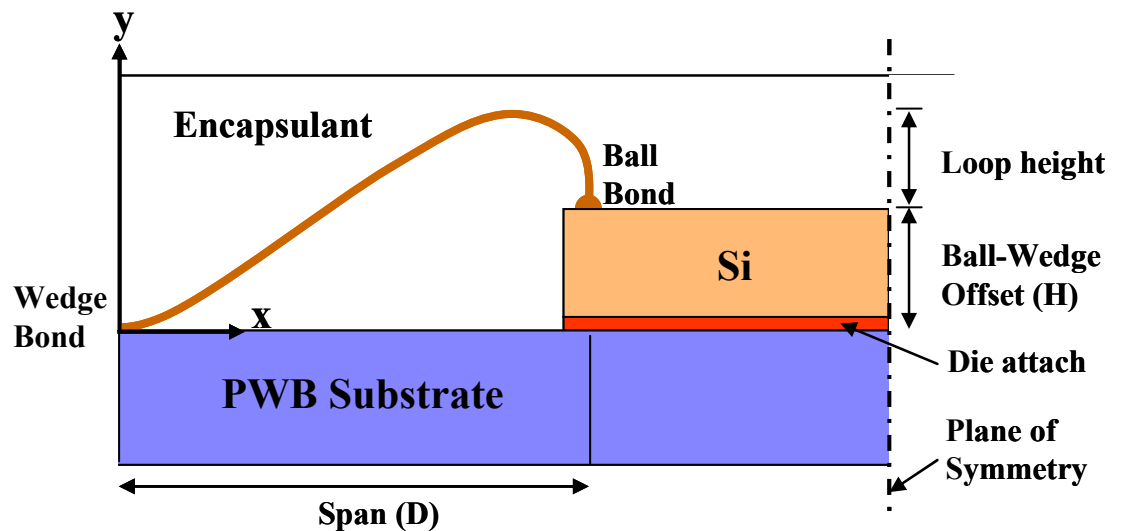


Figure 1.8 Schematic of a typical encapsulated chip

1.8 Nomenclature and Terminology Used

ε = Strain

y_R = Distance of the outermost fiber from the neutral axis in the bond wire

$d\psi$ = Change in angle subtended by the curved bond wire

ψ_i = Take off angle before heating

ψ_f = Take off angle after heating

ρ_i = Curvature of the section at the surface of the bond wire before deformation

ρ_f = Curvature of the section at the surface of the bond wire after deformation

R = Radius of curvature of the neutral axis of the bond wire

r = Radius of curvature of the centroidal axis of the bond wire r = Radius of the cross-section of the bond wire

δs = Change in a small curved length of the bond wire (before and after deformation)

κ_i = Curvature of bond the wire before deformation

κ_f = Curvature of the bond wire after deformation

H = Ball-wedge height offset

D = Span

(d, h) = Coordinates of the point of continuity between the two splines

Θ_c = Slope at (d, h)

Π = Potential energy

κ_1, κ_2 = Curvatures of the two splines

E = Young's Modulus

I = Moment of inertia of the cross-section of the wire

u = Displacement in x-direction, and subscripts I, II and III indicate the sub-domain

L = Half of the length of the die

u_{1sub} , u_{2sub} and u_{die} = adjustable parameters in the RR model, whose values are selected by minimizing the strain energies of the substrate and the die, respectively.

A , B = Adjustable parameters in the RR model, whose values are selected by minimizing the strain energy of the encapsulant

a , b = Fixed constants in the RR model, guided by FEA

v = Displacement in y-direction

v_{die} , $v_{dieattach}$ = Variable parameters in the RR model, whose values are selected by minimizing the strain energies of the die and the die attach, respectively

G , K = Variable parameters in the RR model, whose values are selected by minimizing the strain energy of the encapsulant

g , k_1 , k_2 = fixed constants in the RR model, guided by FEA

U = Total strain energy of the system

W = Work done by external forces

U_{encap} = Strain energy of the encapsulant

U_{wire} = Strain energy of the bond wire

$U_{substrate}$ = Strain energy of the PWB substrate

U_{die} = Strain energy of the Si die

$U_{dieattach}$ = Strain energy of the die attach material.

U_{bend} = Strain energy in the bond wire due to bending

$U_{stretch}$ = Strain energy in the bond wire due to stretching

E = Young's Modulus

ν = Poisson's Ratio

α = Coefficient of Thermal Expansion (CTE)

A = Cross-sectional area

C = Stiffness matrix

E_{encap} = Young's Modulus of the encapsulant

I_{wire} = Moment of inertia of the bond wire cross-section about the neutral axis

A_{wire} = Cross-sectional area of the bond wire

L_{die} = Half the length of the silicon die since the assembly is symmetrical

t_{die} = Thickness of the die

C_{encap} = Stiffness matrix of the encapsulant

2 Optimal Ball-Wedge Wire Profile in Unencapsulated Chips

Procedures for the determination of ball-wedge bonded wire loop profiles are very limited in literature. Groover [Groover et al., 1994] used a statistical design of experiment to define the bonding parameters required to produce the ideal ball bonded wire loop profile for greater than 175 mil wire length. The existing procedures are mostly based on mapping of wire loop profiles. Definition of loop profiles is important for use in analysis tools like finite elements. This chapter describes the methodology for development of an analytical model to determine optimal ball-wedge bonded wire profile in unencapsulated chips. The wire profile obtained is the starting point for the subsequent analysis of stresses developed in the bond wire after encapsulation.

2.1 Ball-Wedge vs. Wedge-Wedge Optimal Profiles

The basic difference between a ball-wedge wire profile and a wedge-wedge wire profile is that ball-wedge wire bond has an infinite slope at the ball bond, where as, the wedge-wedge wire profile has zero slope at both ends. The schematic of ball-wedge and wedge-wedge wire profiles is shown in Figure 2.1. In a ball-wedge wire geometry, for a given set of span (D) and height offset (H), there exists a unique wire profile which will have the minimum elastic strain energy. For any offset (H), the minimum strain energy for the ball-wedge wire profile and the corresponding wire length can be determined as a function of span. The ball-wedge configuration is very different from a wedge-wedge configuration where a straight wire minimizes both wire length and strain energy. Instead, the profile in a wedge-wedge bond is driven by the need for a strain-relief loop to accommodate thermal expansion mismatches.

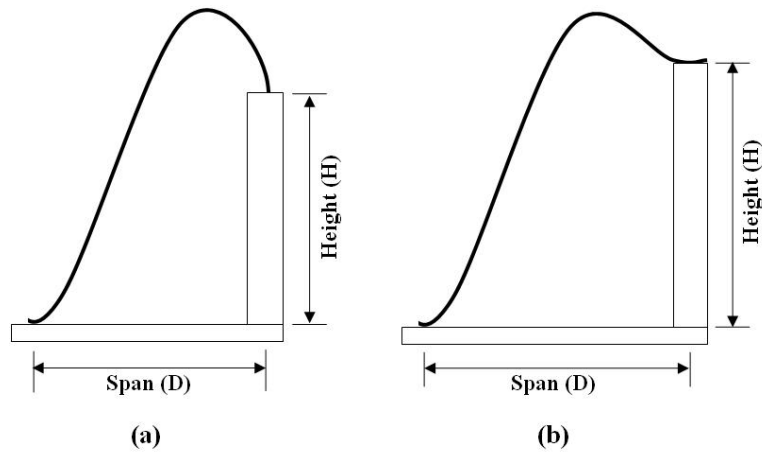


Figure 2.1 (a) Ball-wedge profile (b) Wedge-wedge profile

2.2 Approach

The wire profile is modeled using a piece-wise continuous polynomial function (cubic spline) with appropriate boundary conditions at the two bond sites. A minimum of two splines is necessary to model the entire wire with the appropriate boundary conditions. Depending on the complexity of the profile, more splines may be needed. Only two splines are used for illustrative purpose in this study, and the use of higher number of splines is left to future studies. The model takes two design inputs: ball-wedge height offset (determined by the semiconductor die thickness and the thickness of the die attach material) and the span length (the horizontal distance between the ball and wedge bonds), determined by the package design. An elastic model is used to calculate the flexure-energy in the wire. The model iterates over admissible profiles, which are kinematically compatible with the geometry constraints (offset and span) and finds the correct one by minimizing the strain energy. The large curvatures make this computation intrinsically nonlinear. From the resulting profile, the maximum loop height (an important practical quantity that needs to be set during the wire bonding process) is determined. Once the correct wire profile is known, bending strain and stress along the

wire profile are determined. A similar model was developed at CALCE Electronic Products and Systems Center for wedge-wedge bond configuration in power electronic modules [Meyyappan et al., 2003].

2.2.1 Model

The load transformation model is generally used to predict the bending strains/stresses in the wire. These strains are derived based on the theory of curved beams [Meyyappan, 2004]. Pure bending strain, at any section offset from the neutral axis, is equal to the ratio of change in length to the original length of the curved section, given by,

$$\varepsilon = \frac{y_R (d\psi)}{\rho_i \psi_i} \quad 2.1$$

where, y_R is the distance of the outermost fiber from the neutral axis, $d\psi$ is the change in angle subtended by the curved beam and ρ_i is the curvature of the section at the surface of the beam before deformation (note: - the suffixes i and f are used to denote the variables described before and after deformation of the wire). Hence, $\rho_i \psi_i$ indicates the original length of curved beam. The strains in the upper surface of the wire, given in Eq. 2.1, can be rewritten in terms of the new curvature after deformation, ρ_f and the radius of curvature of the neutral axis, R , by,

$$\varepsilon = \frac{(R - \rho_f) d\psi}{\rho_i \psi_i} \approx \frac{(\bar{r} - \rho_f) d\psi}{\rho_i \psi_i} = \frac{r(\psi_i - \psi_f)}{\rho_i \psi_i} \quad 2.2$$

where, \bar{r} is the radius of curvature of the wire from the centroidal axes (Figure 2.2) and r is the radius of the cross-section of the wire.

The curvature in the beam results in an offset of the neutral axis of the wire from its centroidal axis. The location of the neutral axis follows the condition that the summation of the forces perpendicular to the section must be zero. The location of the neutral axis for a curved beam with a circular cross-section is,

$$R = \frac{\bar{r} + \sqrt{\bar{r}^2 - r^2}}{2} \quad 2.3$$

However, for all practical purposes R can be equated approximately to \bar{r} as done in Eq. 2.2, since the wire has a high radius of curvature when compared to the wire radius.

Assuming no appreciable change in a small curved length of the wire, δs , before and after deformation, the radii of curvatures and the take off angles can be related by the expression,

$$\delta s = \rho_i \psi_i \approx \rho_f \psi_f \quad 2.4$$

From Eq. 2.2 and Eq. 2.4 the expressions for the strains can be rewritten as,

$$\varepsilon = \frac{r(\rho_f - \rho_i)}{\rho_i \rho_f} = -r(\kappa_f - \kappa_i) \quad 2.5$$

where, κ_i and κ_f are the curvatures of the wire which, are inversely proportional to the radius of curvature. It is evident from Eq. 2.5 that the strains are a function of the change in curvature. Hence, one of the most important aspects in the model would be the accurate prediction of the geometry.

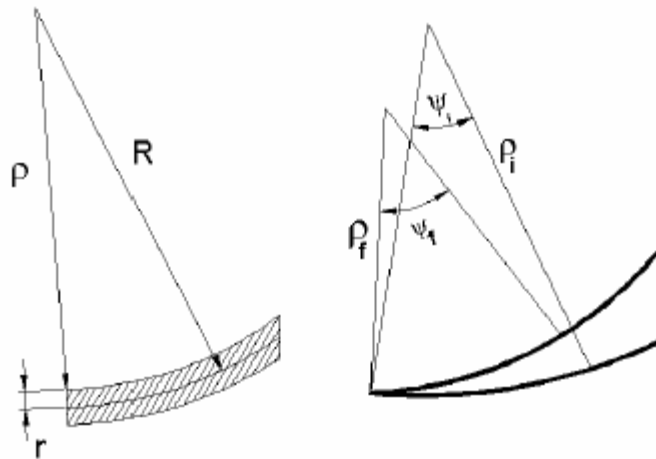


Figure 2.2 Labels used for the derivation of strain in a curved beam

2.2.2 Determination of Wire Profile

The two design parameters for modeling the wire bond profile in a CoB configuration are the ball-wedge height offset, H and the Span, D . The offset is determined by the thickness of the die and the die attach, and the span, D , which is the horizontal distance between the wedge bond and the ball bond, and is determined by the CoB design constraints. The schematic of the wire bonded CoB is shown in Figure 2.3.

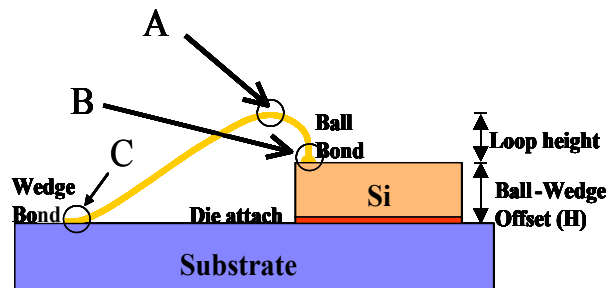


Figure 2.3 Schematic of wire bonded CoB

Wire bond profile can be modeled approximately with strain energy minimization. The approximation is due to the fact that plastic deformations have been ignored in the analysis. The calculated wire profile should resemble the wire bond. This

is achieved by incorporating the boundary conditions physically observed at the wedge and the ball bonds, which are zero slope and infinite slope, respectively.

Cubic splines are the most suitable for strain energy minimization [Carl de Boor, 1978]. A minimum of two splines is necessary to model the entire wire. The spline is parameterized to enforce the continuity and the boundary conditions, especially the infinite slope at the ball bond. Based on the boundary conditions, the parametric forms of the two curves are given by:

$$\begin{aligned} y(u) &= uh - uh(1-u)^2 - (d \times \Theta_c - h)u^2(1-u) \\ x(u) &= ud \end{aligned} \quad 2.6$$

$$\begin{aligned} y(v) &= (1-v)h + vH + [(D-d)\Theta_c - (H-h)]v(1-v)^2 \\ x(v) &= (1-v)d + vD + (D-d)v^2(1-v) \end{aligned} \quad 2.7$$

where, (d, h) is the point of continuity between the two curves, Θ_c is the slope at (d, h) , D is the span and H is the ball-wedge height offset, as shown in Figure 2.4.

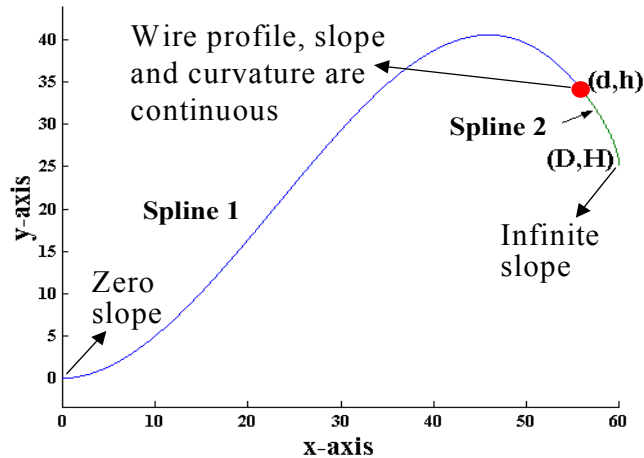


Figure 2.4 Calculated wire profile based strain energy minimization

The cubic splines intrinsically have C^0 and C^1 continuity (C^n continuity: direction and magnitude through the n^{th} derivative are equal at the joining point). C^2 continuity is

obtained by forcing continuity of y'' at (d, h) . This results in an extra equation for Θ_c in terms of the profile parameters:

$$\begin{aligned} \frac{d^2 y_1}{dx_1^2}(d, h) &= \frac{d^2 y_2}{dx_2^2}(d, h) \\ \Rightarrow \frac{4\Theta_c d - 6h}{d^2} &= \frac{4(H - h) - 6(D - d)\Theta_c}{(D - d)^2} \\ \Rightarrow \Theta_c &= \frac{d(D - d)}{(2D + d)} \left[\frac{2(H - h)}{(D - d)^2} + \frac{3h}{d^2} \right] \end{aligned}$$

2.8

The potential energy (Π) can be written as the sum of the bending energy in both splines.

$$\Pi = \frac{EI}{2} \int_0^d \kappa_1^2 (1 + y_1'^2)^{\frac{1}{2}} dx_1 + \frac{EI}{2} \int_d^D \kappa_2^2 (1 + y_2'^2)^{\frac{1}{2}} dx_2 \quad 2.9$$

where, κ_1 and κ_2 are the curvatures of the two splines (Figure 2.4), E is the Young's Modulus and I is the moment of inertia of the cross-section of the wire and the integration is performed along the span, dx . In Eq. 2.9, the potential strain energy is derived based on the straight beam theory, where as curved beam theory was used to derive strain in Eq. 2.5. This simplification is done based on the approximation that the radius of curvature of the neutral axis R , is equal to the radius of curvature of the centroidal axis \bar{r} , since the wire has a high radius of curvature, when compared to the wire radius. For a regular parameterized curve, the curvature for large deformation is obtained by,

$$\kappa = \frac{y''}{(1 + y'^2)^{\frac{3}{2}}} \quad 2.10$$

Using the Raleigh-Ritz technique, by minimizing the potential energy, we obtain two non-linear equations,

$$\frac{\partial \Pi}{\partial d} = 0 \text{ and } \frac{\partial \Pi}{\partial h} = 0 \quad 2.11$$

Solution to these two simultaneous equations provides the two unknown coordinates of the reference point (d , h) for the optimal wire profile. Thus the wire profile with minimum strain energy is obtained. An example of the calculated wire profile is shown in Figure 2.4.

The model iterates over the design space of kinematically feasible profiles (by varying span, D , for a given die height, H ; and vice-versa) and finds the profile which minimizes the strain energy. The term kinematically feasible refers to profiles that satisfy the geometric boundary conditions at the two ends of the wire. The large curvatures in Eqn 10 make this computation intrinsically nonlinear. The model also calculates the corresponding wire length. Alternatively, the length can be specified as a constraint and the corresponding profile can be determined. Detailed results are provided in Section 4.1. Large curvature is observed at the wedge bond, ball bond and in the vicinity of the maximum loop height. The points that show large curvature in the wire can be potential failure sites. All the calculations are performed for 1 mil Au wire with 99.99% purity. It is well known [Harman, 1997] that in ball-wedge thermosonic bonding, there is a region (~ 4 mils) in the wire above the ball bond where the microstructure experiences high grain growth after ball formation and this region is the weakest along the wire. This region is called the heat-affected zone. In this region, there is about 10 percent drop in breaking load for the Au wire. This weakened region, combined with large curvatures at this site, is often a potential site for wire breakage.

3 Prediction of Thermo-Mechanical Stresses in Encapsulated CoB Bond Wire

The die and bond wires in a CoB package are encapsulated to protect them from mechanical and chemical damage. Encapsulation is generally done by dispensing a liquid encapsulant material (usually epoxy based) over the die and wires or by transfer molding. Encapsulants need to undergo a thermal curing process, depending on the type of encapsulant used. Furthermore, the mismatch in the encapsulant CTE properties with the die and substrate can cause fatigue failure in the wire bond interconnections when subjected to thermal cycling loading throughout the life cycle [Pang et al., 1997].

In order to investigate the failure induced due to thermal cycling loading, a quick and efficient stress analysis scheme is essential. In this study a 2D stress analysis model based on Raleigh-Ritz (RR) method is developed. This method is chosen, as it is one of the popular energy-based modeling techniques.

3.1 Development of the Model Guided by 2D Finite Element Analysis (FEA)

The RR method, the displacement fields are approximated by trial functions that satisfy the physical boundary conditions of the problem. The total displacement trial functions are written as a linear weighted combination of simple interpolation functions, and then the weight factors are varied to minimize the total potential energy. The results provide a prediction of thermomechanical strain distributions within the encapsulated gold wire interconnect [Dasgupta, 2002].

Only one half of a CoB assembly is chosen for the analysis because of structural symmetry. The model includes the silicon die, substrate, gold wire interconnect,

encapsulant and die attach material. The initial geometry of the bond wire is determined by the simple RR analysis described in Section 2.1.2.

In order to guide the model development, a 2D FEA model is first developed for such an assembly and subjected to unit temperature thermal loading. The model consists of a PWB substrate, silicon chip, die attach adhesive, wire with ball-wedge bonds and polymer encapsulant, as shown in Figure 3.1. The diameter of the gold wire is 0.025mm (1 mil). The initial condition assumed in the model is a stress free state at a temperature of 175°C, which is also the bonding temperature. Two dimensional finite elements are used to model a single wire-bond interconnection embedded in the encapsulated CoB package. The bond wire is modeled using beam elements. Two-dimensional plane stress elements are used for the rest of the model. The model is assumed to be elastic. The out-of-plane thickness of the plane elements is the pitch between the wire bonds on the CoB. The boundary conditions for the FEA model are, (i) no displacement in x-direction at plane of symmetry, (ii) no warpage displacement in y-direction at the bottom of the PWB substrate. The FEA model with meshed elements is shown in Figure 3.2. A unit temperature change is applied to the model, to observe the deformation in the encapsulant and wire.

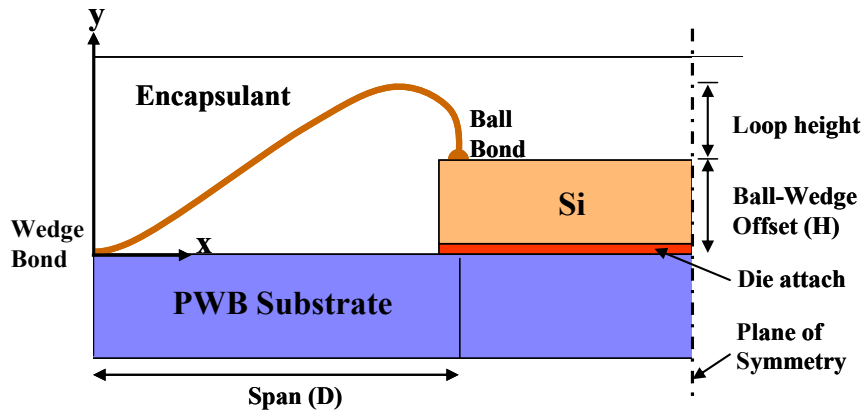


Figure 3.1 Schematic of encapsulated ball-wedge model geometry

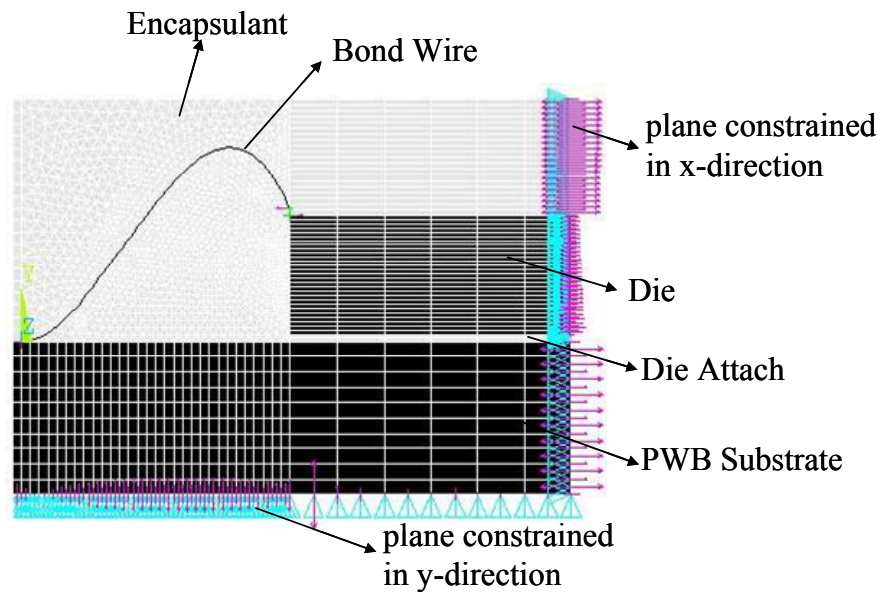
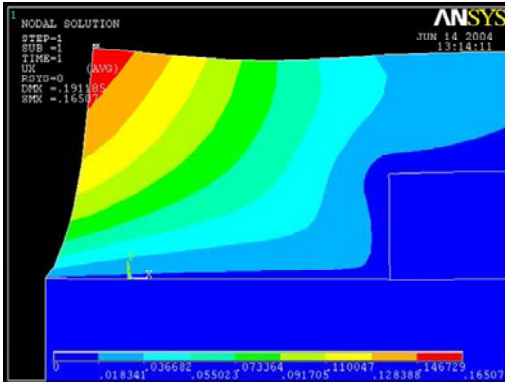
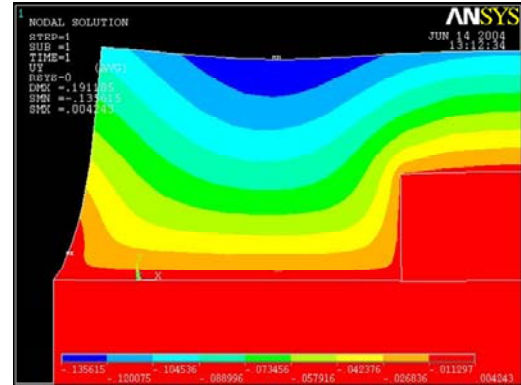


Figure 3.2 FEA model with meshed elements

Contour plots of deformations obtained by the FEA model, as shown in Figure 3.3, are investigated to guide the formulation of the RR displacement fields in the x and y directions.



(a)



(b)

Figure 3.3 Contour plots of displacements in the encapsulant obtained from FEA in (a) x-direction and (b) y-direction

Based on the observed displacement field, the encapsulant in the FEA model is divided into three sub-domains to facilitate the development of accurate trial functions for the RR displacement as shown in Figure 3.4. Displacement functions in each sub-domain are carefully checked for continuity at the interfaces of the sub-domains.

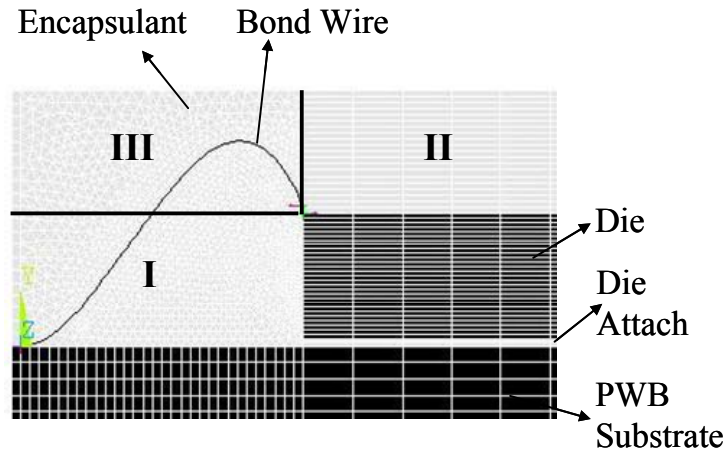


Figure 3.4 Modeling domains in the encapsulant

Guided by the FEA results, the assumed displacement fields, u , in the x-direction in the encapsulant for the RR model are given by the Equations 3.1 - 3.3.

$$u_I = u_{1sub} \left(\frac{x}{D} \right) + A \left[1 - e^{-a \left(\frac{y}{H} \right)} \right] \left(\frac{x-D}{D} \right) \quad 3.1$$

$$u_{II} = u_{1sub} + (u_{2sub} + u_{die}) \left(\frac{x-D}{L} \right) + B \left[1 - e^{-b \left(\frac{y-H}{H} \right)} \right] \left(\frac{x-(D+L)}{L} \right) \quad 3.2$$

$$u_{III} = u_{1sub} \left(\frac{x}{D} \right) + A \left[1 - e^{-a \left(\frac{y}{H} \right)} \right] \left(\frac{x-D}{D} \right) - B \left[1 - e^{-b \left(\frac{y-H}{H} \right)} \right] \left(\frac{x}{D} \right) \quad 3.3$$

where, u is the displacement in x -direction, and subscripts I, II and III indicate the sub-domain. D is the span, H is the ball-wedge height offset and L is the half of the length of the die. u_{1sub} , u_{2sub} and u_{die} are adjustable parameters, whose values are selected by minimizing the strain energies of the substrate and the die, respectively. A and B are adjustable parameters whose values are selected by minimizing the strain energy of the encapsulant. In this study, a and b are fixed constants, guided by FEA. The detailed derivation of a and b is given in Appendix A. Equations 3.1, 3.2 and 3.3 satisfy interface continuity at the interfaces of sub-domains I, II and III, and the following boundary conditions as follows:

$$@ x=0, y=0 \quad u_I = 0$$

$$@ y=H \quad u_I = u_{III}$$

$$@ x=D \quad u_I = u_{1sub}$$

$$@ x=D \quad u_{II} = u_{III}$$

$$@ x=D+L \quad u_{II} = u_{1sub} + u_{2sub} + u_{die}$$

$$@ x=D, y=H \quad u_I = u_{II} = u_{III} = u_{1sub}$$

A comparison between the FEA and the assumed displacement fields (u) in the x -direction is shown in the Figure 3.5. Although the RR assumed displacement field is

simplified, it does a reasonable job of mimicking the detailed FEA results. As discussed later the key issue is that this RR displacement field should produce wire strains that agree reasonably well with the FEA results.

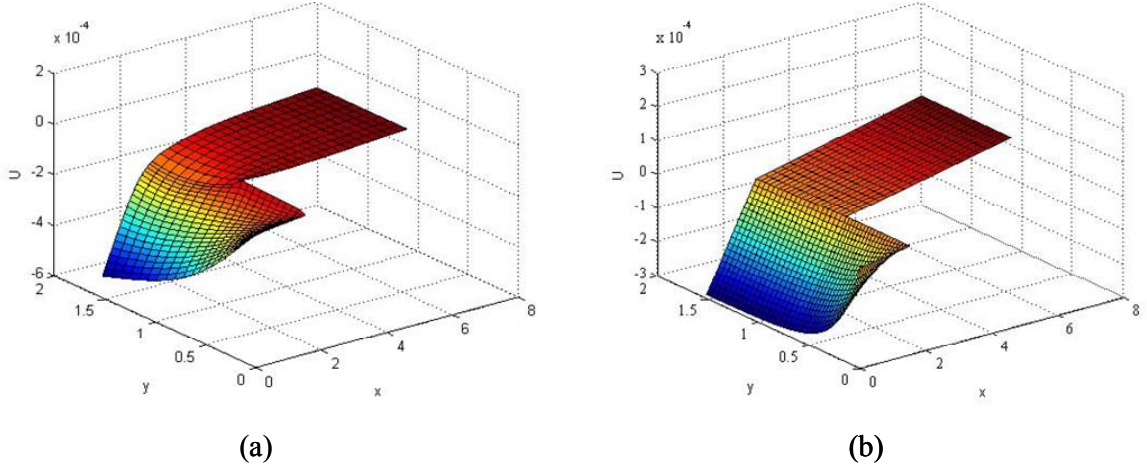


Figure 3.5 Displacement profiles in the encapsulant in the x-direction from (a) FEA and (b) the RR model

The assumed displacement fields, v , in the y -direction in the encapsulant, for the RR model are given by Equations 3.4 - 3.6.

$$v_I = (v_{die} + v_{dieattach}) e^{k_1 + \frac{k_2}{H}} \left(\frac{y}{H} \right) + G \left[1 - e^{-g \left(\frac{D-x}{D} \right)} \right] \left(\frac{y}{H} \right) \quad 3.4$$

$$v_{II} = \left[v_{die} + v_{dieattach} + K \left(\frac{y-H}{H} \right) \right] e^{k_1 \left(\frac{D+L-x}{L} \right) + k_2 \left(\frac{1}{y} \right)} \quad 3.5$$

$$v_{III} = (v_{die} + v_{dieattach}) e^{k_1 + \frac{k_2}{y}} + K \left(\frac{y-H}{H} \right) e^{k_1 + \left(\frac{k_2}{y} \right)} + G \left[1 - e^{-g \left(\frac{D-x}{D} \right)} \right] \left(\frac{H}{y} \right) \quad 3.6$$

where, v is the displacement in y -direction, and subscripts I, II and III indicate the sub-domain. D , H and L have been defined earlier. v_{die} and $v_{dieattach}$ are variable parameters whose values are selected by minimizing the strain energies of the die and the die attach,

respectively. G and K are variable parameters whose values are selected by minimizing the strain energy of the encapsulant. g , k_1 and k_2 are fixed constants guided by FEA. The detailed derivation of g , k_1 and k_2 is given in Appendix A. Equations 3.4 - 3.6 satisfy interface continuity at the interfaces of domains I, II and III, and the boundary conditions as follows:

$$@ y=0 \quad v_I = 0$$

$$@ y=H \quad v_I = v_{III}$$

$$@ x=D, y=H \quad v_I = v_{II} = v_{III} = (v_{die} + v_{dieattach}) \exp(k_1 + k_2/H)$$

$$@ x=D \quad v_{II} = v_{III}$$

A comparison between the FEA and the assumed displacement fields (v) in the y -direction is shown in Figure 3.6.

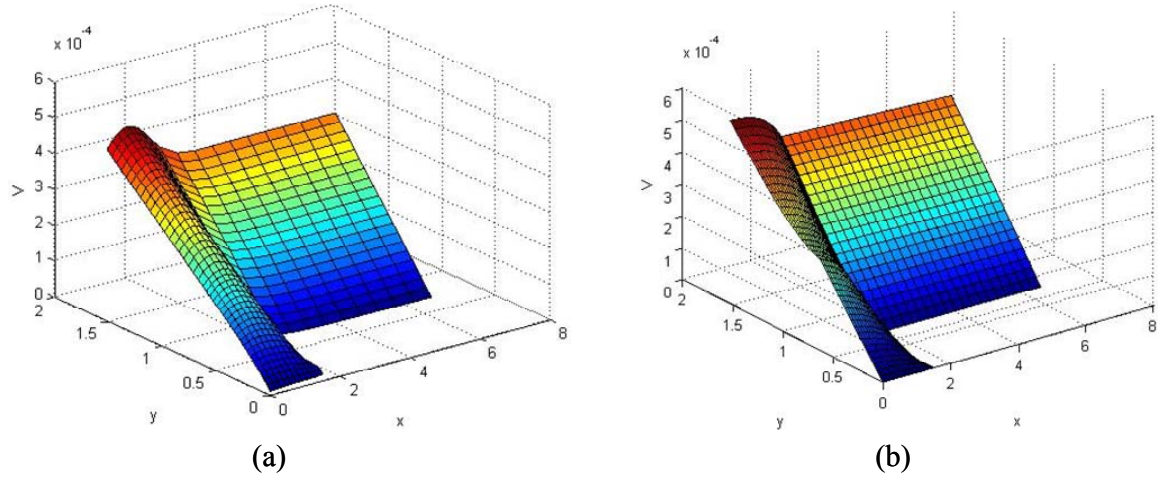


Figure 3.6 Displacement profiles in the encapsulant in the y -direction from (a) FEA and (b) the RR model

In the RR method, these displacement fields are next used to estimate the potential energy. The total mechanical potential energy Π is given by,

$$\Pi = U - W \tag{3.7}$$

where, U is the total strain energy of the system, W is work done by external forces. $W = 0$ for thermal loading. Therefore the total potential energy is the sum of the strain energies in the different constituents of the system.

$$\Pi = U_{encap} + U_{wire} + U_{substrate} + U_{die} + U_{dieattach} \quad 3.8$$

where, U_{encap} is the strain energy of the encapsulant, U_{wire} is the strain energy of the Au wire, $U_{substrate}$ is the strain energy of the PWB substrate, U_{die} is the strain energy of the Si die and $U_{dieattach}$ is the strain energy of the die attach material. The strain energy in the bond wire is composed of contributions due to the bending (U_{bend}) and the stretching ($U_{stretch}$) in the gold wire.

$$U_{wire} = U_{bend} + U_{stretch} \quad 3.9$$

The strain energy terms in Eq. 3.8 are given by the following equations:

$$U_{encap} = \frac{1}{2} \int_{\Omega_1} (\varepsilon_{total} - \varepsilon_{thencap})^T \cdot C_{encap} \cdot (\varepsilon_{total} - \varepsilon_{thencap}) dV \quad 3.10$$

$$U_{bend} = \frac{1}{2} \int_0^L E_{wire} I_{wire} \left(\frac{\partial^2 V_n}{\partial s^2} \right)^2 ds \quad 3.11$$

$$U_{stretch} = \frac{1}{2} \int_0^L E_{wire} A_{wire} (\varepsilon_{ss} - \varepsilon_{thwire})^2 ds \quad 3.12$$

$$U_{substrate} = \frac{1}{2} \int_{\Omega_2} E_{substrate} \left(\frac{u_{substrate}}{L_{substrate}} - \alpha_{substrate} (\Delta T) \right)^2 dV \quad 3.13$$

$$U_{die} = \frac{1}{2} \int_{\Omega_3} E_{die} \left(\frac{u_{die}}{L_{die}} - \alpha_{die} (\Delta T) \right)^2 dV + \frac{1}{2} \int_{\Omega_3} E_{die} \left(\frac{v_{die}}{t_{die}} - \alpha_{die} (\Delta T) \right)^2 dV \quad 3.14$$

$$U_{dieattach} = \frac{1}{2} \int_{\Omega_3} E_{dieattach} \left(\frac{\nu_{dieattach}}{t_{dieattach}} - \alpha_{dieattach} (\Delta T) \right)^2 dV + \frac{1}{2} \int_{\Omega_3} \frac{E_{dieattach}}{2(1+\nu_{dieattach})} \left(\frac{u_{die} - u_{substrate}}{t_{dieattach}} \right)^2 dV \quad 3.15$$

$$\text{where, } C_{encap} = \frac{E_{encap}}{1-\nu_{encap}^2} \begin{bmatrix} 1 & \nu_{encap} & 0 \\ \nu_{encap} & 1 & 0 \\ 0 & 0 & \frac{1-\nu_{encap}}{2} \end{bmatrix}, \quad \varepsilon_{thencap} = \begin{bmatrix} \alpha_{encap} \\ \alpha_{encap} \\ 0 \end{bmatrix} \Delta T,$$

$$\varepsilon_{total} = \begin{bmatrix} \frac{\partial u}{\partial x} \\ \frac{\partial v}{\partial y} \\ \frac{\partial u}{\partial y} + \frac{\partial v}{\partial x} \end{bmatrix}, \quad V_n = -u \sin \theta + v \cos \theta = -u \frac{dy}{ds} + v \frac{dx}{ds}$$

$$\varepsilon_{ss} = \varepsilon_{xx} \cos^2 \theta + \varepsilon_{yy} \sin^2 \theta + \gamma_{xy} \sin \theta \cos \theta$$

E, ν and α are the constants of Young's Modulus, Poisson's Ratio and CTE of each material, respectively and the subscript shows the material, for e.g., E_{encap} is the Young's Modulus of the encapsulant. I_{wire} is the moment of inertia of the gold wire, and A_{wire} being the cross-sectional area. L_{die} is only half the length of the silicon die since the assembly is symmetrical and t_{die} is the thickness of the die. C_{encap} is the stiffness matrix of the encapsulant, ε_{total} is the total strain in the encapsulant, ε_{encap} is the thermal strain in the encapsulant, $\Delta T = -1^\circ\text{C}$, V_n is the deflection in the wire perpendicular to the axis of the wire, ε_{ss} is the axial strain in the wire. In Eq. 3.11, the bending energy in the wire is derived based on the straight beam theory. This simplification is done based on the assumption that the radius of curvature of the neutral axis R, is equal to the radius of

curvature of the centroidal axis \bar{r} , since the wire has a high radius of curvature when compared to the wire radius.

Equations 3.10 - 3.12 represent the generalized strain energy functions used in this analysis. There are several intermediate equations that arise due to the facts that there are two cubic splines which are parametric and three domains in the encapsulant. These intermediate equations are discussed in brief here for domain I in the encapsulant. The detailed derivations for all the functions in their domains are discussed in Appendix B. The strain energies described in Equations 3.11 and 3.12, in the wire are due to bending and stretching of the wire under a thermal load. For domain I, Eq. 3.11 results in the following expression,

$$U_{bend_{1a}} = \frac{1}{2} \int_0^{l_{1a}} E_{wire} I_{wire} \left(\frac{\partial^2 V_{n_{1a}}}{\partial s_{1a}^2} \right)^2 ds_{1a} \quad 3.16$$

where, l_{1a} is the length of the wire in domain I and is equal to parameter u for $y_1(u) \leq H$.

In the subscript '1a', '1' represents the first cubic spline and 'a' represents the domain I.

Furthermore, Eq. 3.16 also accounts for the respective displacement fields, u_1 and v_1 .

Therefore, in the parametric form,

$$\begin{aligned} \frac{\partial^2 V_{n_{1a}}}{\partial s_{1a}^2} &= \frac{\partial}{\partial s_{1a}} \left(\frac{\partial V_{n_{1a}}}{\partial s_{1a}} \right) = \frac{d}{du} \left(\frac{\partial V_{n_{1a}}}{\partial s_{1a}} \right) \frac{du}{ds_{1a}} = \frac{d}{du} \left(\frac{dV_{n_{1a}}}{du} \frac{du}{ds_{1a}} \right) \frac{du}{ds_{1a}} \\ V_{n_{1a}} &= -u_{1a} \sin \theta_{1a} + v_a \cos \theta_{1a} = -u_{1a} \left(\frac{\partial y_{1a}}{\partial s_{1a}} \right) + v_{1a} \left(\frac{\partial x_{1a}}{\partial s_{1a}} \right) \\ &= -u_{1a} \left(\frac{dy_{1a}}{du} \frac{du}{ds_{1a}} \right) + v_{1a} \left(\frac{dx_{1a}}{du} \frac{du}{ds_{1a}} \right) \end{aligned} \quad 3.17$$

where, $ds_{1a} = \sqrt{(dx_{1a})^2 + (dy_{1a})^2} du$, u_{1a} is u_1 , v_{1a} is v_1 .

In Eq. 3.12, ε_{ss} in domain I can be parametrically shown as,

$$\begin{aligned}
\varepsilon_{ss_{1a}} &= \varepsilon_{xx_{1a}} \text{Cos}^2\theta_{1a} + \varepsilon_{yy_{1a}} \text{Sin}^2\theta_{1a} + \gamma_{xy_{1a}} \text{Sin}\theta_{1a} \text{Cos}\theta_{1a} \\
&= \frac{\partial u_{1a}}{\partial x_{1a}} \left(\frac{\partial x_{1a}}{\partial s_{1a}} \right)^2 + \frac{\partial v_{1a}}{\partial y_{1a}} \left(\frac{\partial y_{1a}}{\partial s_{1a}} \right)^2 + \left(\frac{\partial u_{1a}}{\partial y_{1a}} + \frac{\partial v_{1a}}{\partial x_{1a}} \right) \left(\frac{\partial y_{1a}}{\partial s_{1a}} \right) \left(\frac{\partial x_{1a}}{\partial s_{1a}} \right) \\
&= \left(\frac{du_{1a}}{du} \frac{du}{dx_{1a}} \right) \left(\frac{dx_{1a}}{du} \frac{du}{ds_{1a}} \right)^2 + \left(\frac{dv_{1a}}{du} \frac{du}{dy_{1a}} \right) \left(\frac{dy_{1a}}{du} \frac{du}{ds_{1a}} \right)^2 + \\
&\quad \left(\frac{du_{1a}}{du} \frac{du}{dy_{1a}} + \frac{dv_{1a}}{du} \frac{du}{dx_{1a}} \right) \left(\frac{dy_{1a}}{du} \frac{du}{ds_{1a}} \right) \left(\frac{dx_{1a}}{du} \frac{du}{ds_{1a}} \right)
\end{aligned} \tag{3.18}$$

Accordingly, $\varepsilon_{\text{total}}$ in Eq. 3.10 can be represented as follows,

$$\varepsilon_{\text{total}_I} = \begin{bmatrix} \frac{\partial u_I}{\partial x_I} \\ \frac{\partial v_I}{\partial y_I} \\ \frac{\partial u_I}{\partial y_I} + \frac{\partial v_I}{\partial x_I} \end{bmatrix} \tag{3.19}$$

where, x_I represents $x = 0$ to $x = D$, and y_I represents $y = 0$ to $y = H$. Eqns 3.16 - 3.18 repeat for domain III, and Eq. 3.19 repeats for domains II and III. The resulting expressions are discussed in detail in Appendix B.

Minimization of the potential energy with respect to all the parameters in Eqns. 3.1 – 3.6 results in values for these adjustable coefficients. Let the unknown coefficients form the vector of degrees of freedom, \vec{X} .

$$\mathbf{X} = \left[\mathbf{A} \quad \mathbf{B} \quad u_{1sub} \quad u_{2sub} \quad u_{die} \quad v_{die} \quad v_{dieattach} \quad \mathbf{K} \quad \mathbf{G} \right] \tag{3.20}$$

Thus energy minimization leads to the stationary condition:

$$\frac{\partial \Pi}{\partial X_i} = 0 \quad i = 1 - 9 \tag{3.21}$$

This leads to 9 linear, simultaneous equations in 9 unknowns, and can be solved using standard linear algebra techniques. To verify that the energy minimization leads to a stationary condition, strain energy was plotted against each parameter, X_i . All the strain

energy plots have global minimum and are shown in Appendix C. The result of this analysis is a quantitative estimate of the displacement field. The worst strain in the outer fiber of the gold wire is given by,

$$\left| \mathcal{E}_{wire} \right| = \left| \mathcal{E}_{ss} - \mathcal{E}_{th} \right| + \left| \mathcal{E}_{bend} \right| \quad 3.22$$

where, \mathcal{E}_{wire} is the total mechanical strain in the wire, \mathcal{E}_{ss} is the axial strain in the wire, \mathcal{E}_{th} is the thermal strain in the wire and \mathcal{E}_{bend} is the strain in the wire due to flexure. Eq. 3.18 can be evaluated at any given distance from the neutral axis of the wire.

4 Results and Discussion

The 2D Raleigh-Ritz (RR) analysis presented in chapter 3 was carried out for a unit temperature change (cool-down), $\Delta T = -1^\circ\text{C}$. Parametric studies were conducted using the RR model, for various design geometries, encapsulants and die attach materials; discussed later in this section. The results were compared with detailed 2D Finite Element Analysis (FEA). A comparison of test data with the FEA model and with the RR model is also discussed in this chapter.

4.1 Determination of Wire Profile and Loop Height in Unencapsulated Ball-Wedge Wire-Bonds

The usefulness of this simple elastic model lies in the ability to perform parametric sensitivity analysis to determine few practical quantities, like optimal loop profile for a CoB design and loop height for a given span and offset. The optimal loop height is an important parameter that needs to be set as an input during wire bond manufacturing. For a given set of D and H , there exists a unique set of d and h , for which the wire profile will have the minimum elastic strain energy. For any offset (H), the minimum strain energy for the wire profile and the corresponding wire length can be determined as a function of span. The result of this study is presented in Figure 4.1 as an example, for $H=25$ mils, because this is a common industry standard. Clearly, the flexural rigidity EI in Equation (2.9), will cancel out of Equations (2.11) during the minimization, and hence will not affect the predicted wire profile. Similar plots can be generated for any H . In Figure 4.1, the elastic strain energy of the wire profile decreases asymptotically

with increase in the span and the corresponding wire length increases almost linearly with the span.

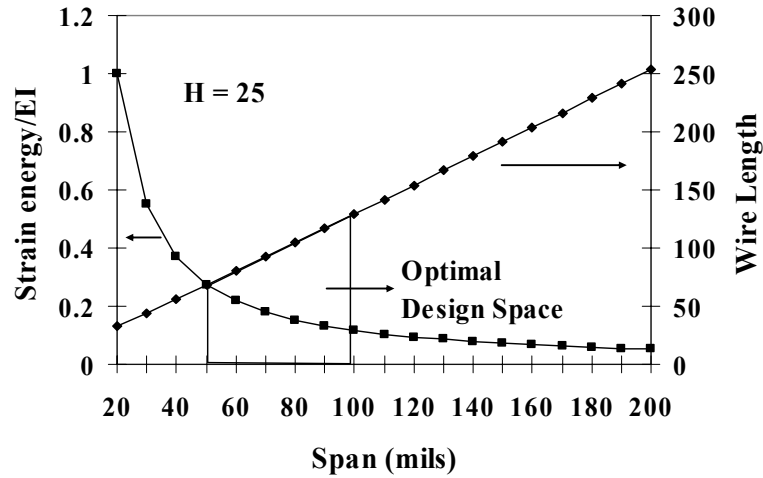


Figure 4.1 Determination of optimal wire profile

The information in Figure 4.1 can be used to design an optimal span that reduces the strain energy without an undue increase in the wire length. The wire length introduces parasitic effects due to resistance and inductance, and should hence be minimized. Moreover, the cost of the gold (99.99% pure gold) also increases as the length of the wire increases. Thus an optimum wire profile should attempt to minimize strain energy, resistance, inductance and cost. This problem definition is very different from a wedge-wedge configuration where a straight wire minimized both wire length and strain energy. Instead, the profile in a wedge-wedge bond is driven by the need for a strain-relief loop to accommodate thermal expansion mismatches.

Also, based on the minimum strain energy profile, for any span and height offset, the loop height can be estimated. The loop height is the difference between the peak of the wire and the height offset (H). Figure 4.2 shows the loop height vs. span for minimum strain energy wire profiles with three given height offsets. Based on this analysis, it is

found that loop height is approximately 25% of the span. This conclusion is consistent with the industry observation in open cavity packages [Harman, 1997], and qualitatively provides some confidence that the elastic approximation is acceptable for this problem.

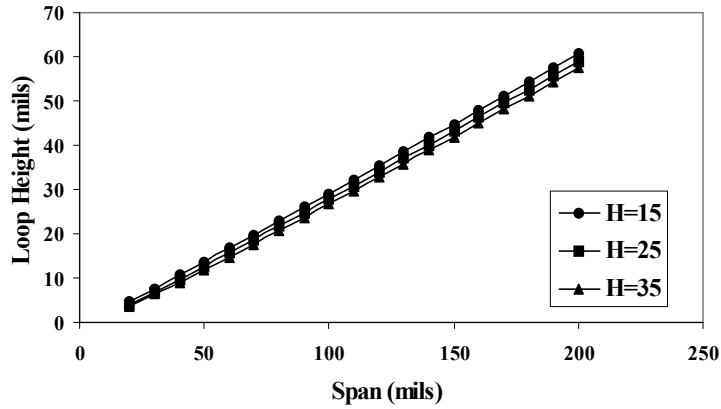


Figure 4.2 Loop height vs. span for minimum strain energy wire profiles

Optimal wire bond geometries predicted by this model, are shown in Figure 4.3, for varying spans (at constant offset of 25 mils) and varying offsets (at a constant span of 40 mils).

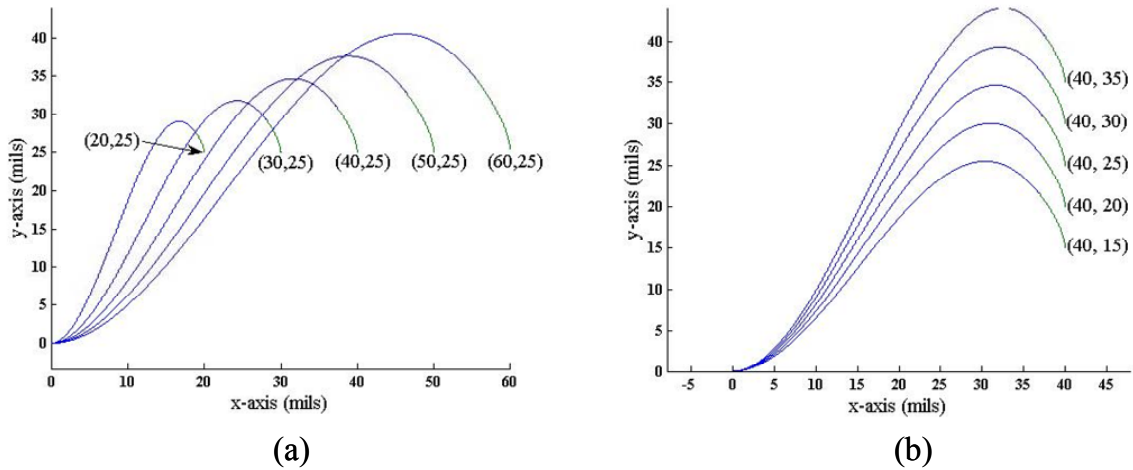


Figure 4.3 Wire profiles for (a) various spans ($H=25$ mils) and (b) various offsets ($D=40$ mils)

A parametric study has been done to see the effect of span and height offset on (i) curvature at the wedge bond (C); (ii) curvature at the top of the wire (A); (iii) curvature at the ball bond (B); (iv) wire length; and (v) loop height. This parametric study has been

illustrated in Figure 4.4 for changes in wire span (while holding the die height constant at 25 mils) and in Figure 4.5 for changes in die height (while holding the wire span constant at 40 mils). All values on the y axes are normalized with respect to the corresponding values for a reference geometry (40 mil span or 25 mil die height). As expected, for a given span, as the die height increases, the curvatures at the potential failure sites increase.

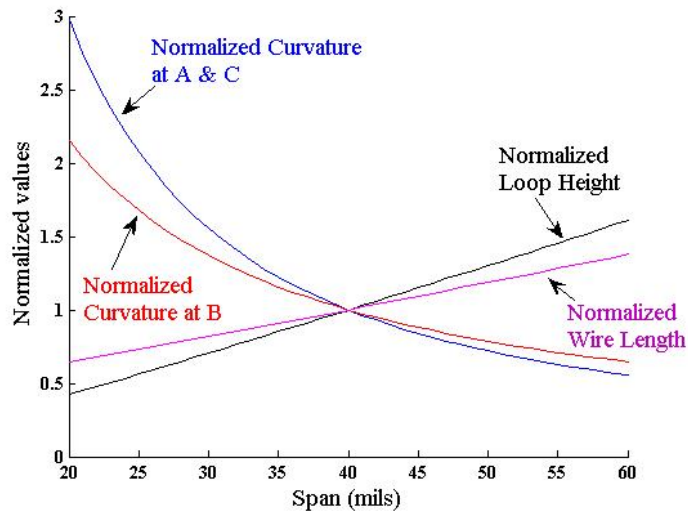


Figure 4.4 Parametric analysis for various spans ($H=25$ mils)

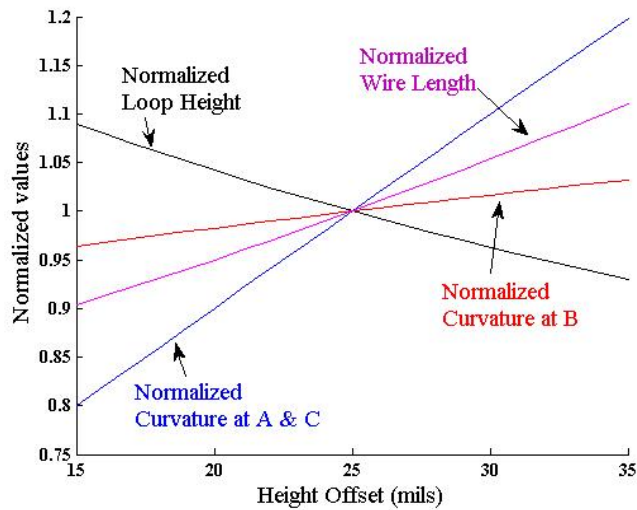


Figure 4.5 Parametric analysis for various height offsets ($D=40$ mils)

4.2 Comparison of the RR model with FEA for Thermomechanical Analysis of Encapsulated Ball-Wedge Wire-Bond

For each CoB configuration analyzed by the RR model described in Section 3, an equivalent detailed FEA solution was obtained, to verify the validity of the semi-analytical RR model. The model parameters are given in Table 4.1. As shown in Figure 4.6, the RR model predicts that the bending strains are an order of magnitude smaller than the axial strains. This result is confirmed by the FEA. The strain distributions predicted by the RR model agree qualitatively with the detailed FEA. However, the magnitude of elastic strain near the wedge bond predicted by the RR model is greater than that predicted by the FEA strains, because of the approximations in the assumed displacement fields in the RR model. This difference gradually decreases along the wire profile towards the ball bond.

Table 4.1 Design Parameters to compare the RR model with FEA

Geometric variable	Values (mils)		
Span	56		
Die thickness	25		
Die attach thickness	1.5		
Wire diameter	1		
Die length	200		
Materials	E (GPa)	CTE (ppm/°C)	Poisson's Ratio ν
Wire	78	14.2	-
Silicon die	115	6	-
Substrate	120	10	-
Encapsulant	10	80	0.4
Die attach	6	56	0.4

The wedge bond is at $x=0$ and the ball bond is at $x=x_{\max}$. The total elastic strain along the wire profile is compared between FEA and the RR model in Figure 4.7. The

maximum axial and total strains in the wire interconnect are predicted to occur at the ball bond for most of the configurations examined.

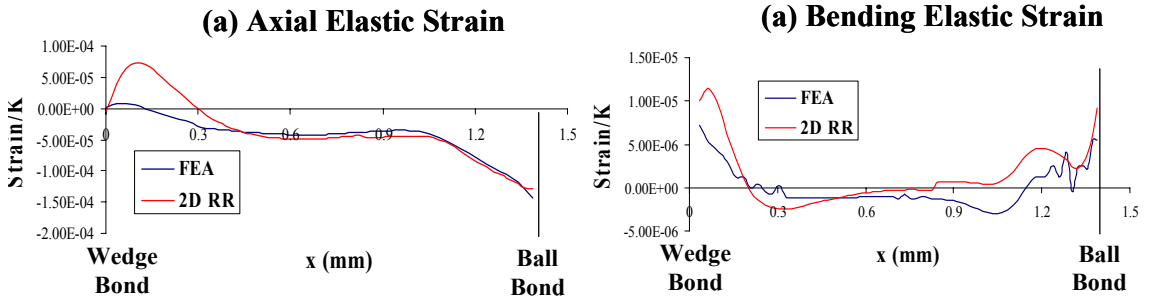


Figure 4.6 Comparison of (a) axial and (b) bending elastic strains in FEA and the RR model

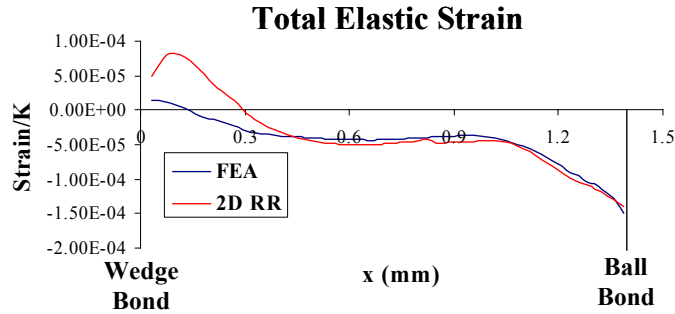


Figure 4.7 Comparison of total elastic strains between FEA and the RR model

4.3 Parametric Studies

Parametric studies were performed to verify the range of validity of the RR model. The major parameters varied are the Young's Modulus of the encapsulant, CTE of the encapsulant and the design inputs D and H of the wire-bond geometry. The material properties of Au ($E_{Au} = 78 \text{ GPa}$, $\alpha_{Au} = 14.2 \text{ ppm}^{\circ}\text{C}$) wire and Si ($E_{die} = 115 \text{ GPa}$, $\alpha_{die} = 6 \text{ ppm}^{\circ}\text{C}$) die, and $\nu_{encapsulant} = 0.4$ and $\nu_{dieattach} = 0.4$ were kept constant throughout the course of the analysis. The die length was 10 mm and the wire diameter was 25 μm (1 mil), for all the runs. Table 4.2 describes the parametric variations in the analysis conducted to validate the RR model with FEA.

Table 4.2 Parametric variations used to validate RR model

Young's Modulus, E (GPa)	CTE (ppm/°C)			Parameters held Constant
3	100	150	200	Span = 56 mils Die thickness = 25 mils Die Attach thickness = 1.5 mils $E_{dieattach} = 6 \text{ GPa}$, $\alpha_{dieattach} = 56 \text{ ppm/}^\circ\text{C}$ Substrate thickness = 60 mils $E_{substrate} = 120 \text{ GPa}$, $\alpha_{substrate} = 10 \text{ ppm/}^\circ\text{C}$
6	20	30		
6.5	55			
9	20	30		
10	10	80		
13.5	105			
17	10			
24	1	10	50	
0.07, 0.1, 0.4, 0.7, 1, 4, 10, 24	100			Span = 50 mils Die thickness = 25 mils Die Attach thickness = 1.5 mils $E_{dieattach} = 1.6 \text{ GPa}$, $\alpha_{dieattach} = 156 \text{ ppm/}^\circ\text{C}$ Substrate thickness = 62 mils $E_{substrate} = 16.5 \text{ GPa}$, $\alpha_{substrate} = 59 \text{ ppm/}^\circ\text{C}$
Span (mils)	Die Thickness (mils)			
40	20	25	30	$E_{encapsulant} = 10 \text{ GPa}$, $\alpha_{encapsulant} = 80 \text{ ppm/}^\circ\text{C}$ Die Attach thickness = 1.5 mils $E_{dieattach} = 1.6 \text{ GPa}$, $\alpha_{dieattach} = 156 \text{ ppm/}^\circ\text{C}$ Substrate thickness = 62 mils $E_{substrate} = 16.5 \text{ GPa}$, $\alpha_{substrate} = 59 \text{ ppm/}^\circ\text{C}$
60				
80				

Parametric analysis was carried out for various material properties (substrate, encapsulant and die attach) and different spans and die thicknesses. The resulting maximum elastic strains obtained from the RR model were compared with the maximum elastic strains obtained from FEA for corresponding values of the design parameters. The maximum strains were obtained at the ball bond estimated at a distance of 99% of the span. The RR model agrees well quantitatively with detailed FEA for stiff encapsulants, $E \geq 3 \text{ GPa}$, and for wire diameter under $50 \mu\text{m}$ (2 mils). The maximum strain values obtained from the RR model and from the FEA were plotted against each other in Figure

4.8. It can be seen that the RR model agrees quantitatively well with FEA, confirmed by the proximity of the plot points to the 45° line in the plot. For compliant encapsulants ($E < 3$ GPa), and for thick wires ($d > 2$ mils), the RR model overpredicts the strains compared to the strains predicted by detailed FEA. The disagreement arises because the simple displacement fields chosen for the RR model are not able to capture the local displacement gradients in the encapsulant around wire.

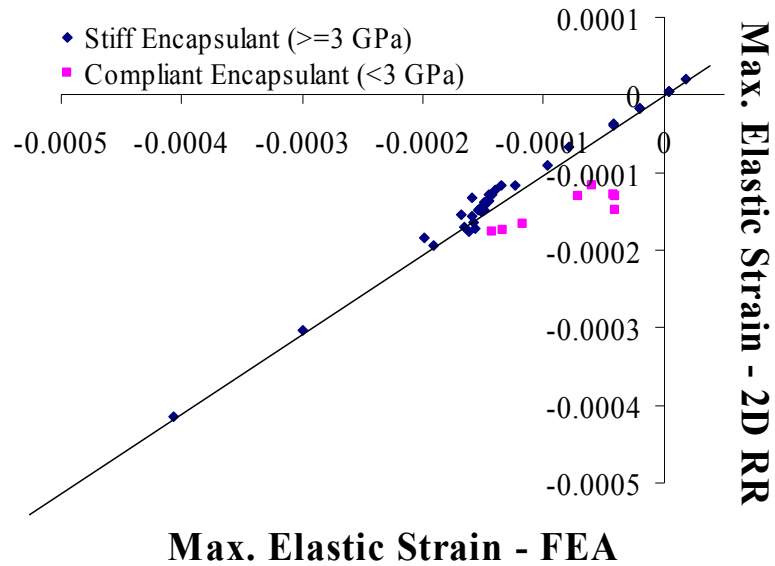


Figure 4.8 Comparison of maximum elastic strain between FEA and the RR model

To further visualize the effect of the Young's Modulus of the encapsulant on the accuracy of the proposed model, the percentage difference between the FEA elastic strains and the RR model elastic strains at the ball bond, is plotted in Figure 4.9 against the Young's Modulus of the various encapsulants used for the analysis. As expected, the % difference increases with the compliance of the encapsulant. For encapsulants with Young's modulus between 3 and 24 GPa, the error values vary between 1.3% and 16.7%. As the value of E falls below 3 GPa, the error increases rapidly to 100%.

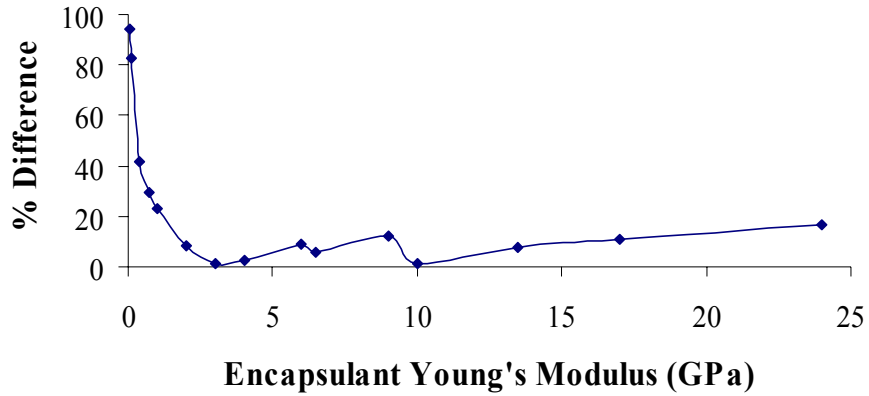


Figure 4.9 Variation of % difference between the FEA and the RR model (in max. elastic strain) with Young's Modulus of Encapsulant

The effect of geometric inputs, span (D) and height offset (H), on the maximum elastic strain at the ball bond is studied. Figure 4.10 shows a contour plot of the maximum elastic strain at the ball bond with span on the x-axis and height offset on the y-axis. It can be seen that the max. elastic strain at the ball bond decreases by 14% with 50% increase in span (D), and increases by 6% with 25% increase in offset height (H). This trend is in qualitative agreement with trends in minimum strain energy of unencapsulated wires.

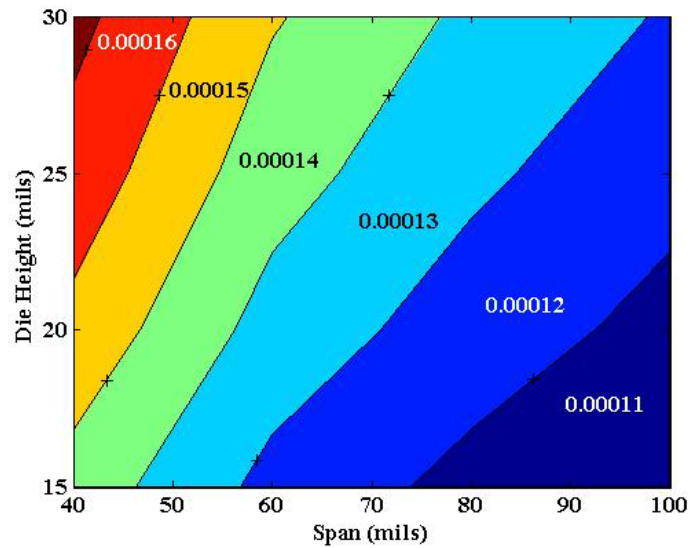


Figure 4.10 Contour plot of elastic strain for change in die height (H) and span (D)

To see the effect of Young's Modulus and CTE of encapsulant on the maximum elastic strain at the ball bond a contour plot, shown in Figure 4.11, with Young's Modulus on the x-axis and CTE on the y-axis is plotted. Stiff encapsulants have lower CTEs, hence, for parametric evaluation the area below the shaded region in the plot should be considered.

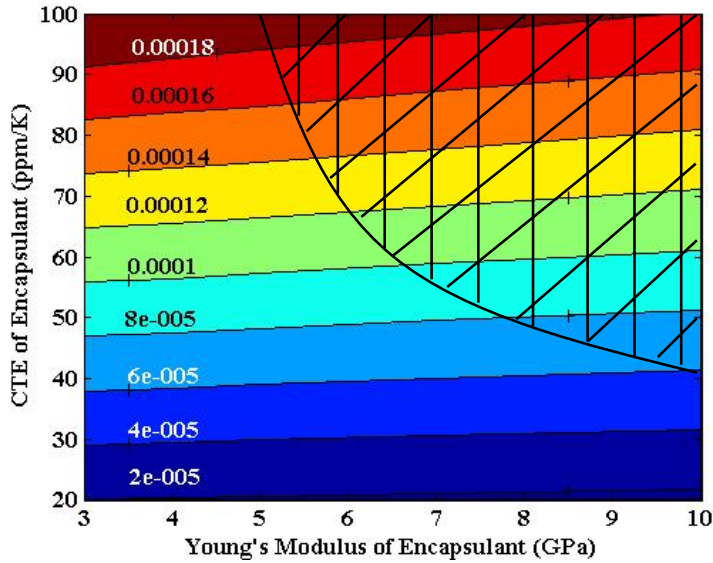


Figure 4.11 Contour plot of elastic strain for change in CTE and Young's Modulus of the encapsulant

The elastic strain at the ball bond increases with an increase in the encapsulant CTE. However, the study shows that the strain decreases with increase in the Young's modulus of the encapsulant. This result is inconsistent with the FEA. Axial elastic strains along the span for two CoBs with different encapsulant Young's Modulus (3 and 10 GPa) were compared between the FEA and the RR model, shown in Figure 4.12. The magnitude of strain at the ball bond predicted by the FEA for a CoB with a encapsulant Young's modulus 10 GPa is greater than that of 3 GPa. But, the RR model predicts contrarily. This is due to the simple displacement fields chosen. This error in the RR

model can be minimized by improving the chosen trial displacement fields both in x and y directions.

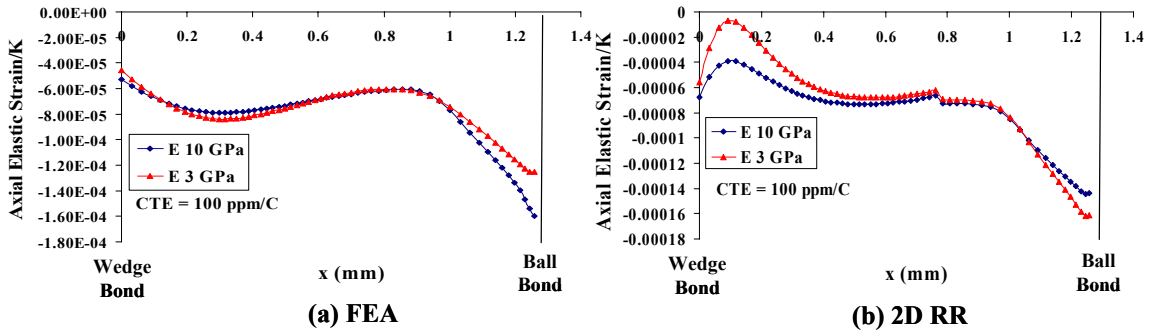


Figure 4.12 Axial strain along the span predicted by (a) FEA and (b) the RR model for CoBs with different encapsulant Young's Modulus

To further visualize the effect of the diameter of the bond wire on the accuracy of the proposed model, the percentage difference between the FEA elastic strains and the RR model elastic strains at the ball bond, is plotted in Figure 4.13 against the diameter of the bond wire. For CoBs with wire diameters less than 2 mils, the error values vary between 8.5% and -11.5%. As the value of diameter increases beyond 2 mils, the error increases rapidly to -100%.

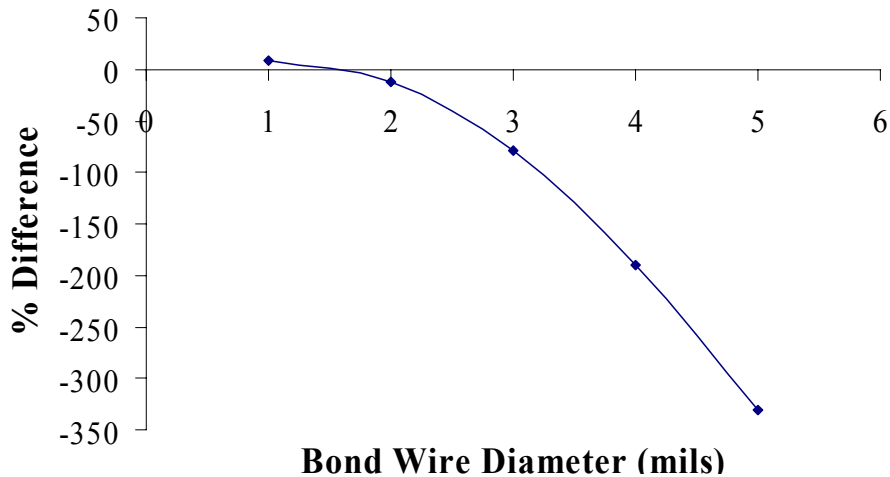


Figure 4.13 Variation of % difference between FEA and the RR model (in max. elastic strain) with diameter of the bond wire

4.4 Comparison of Test Results [APL, 2005] with Model Predictions

Test samples with several different encapsulants, die attaches and substrates were fabricated and subjected to thermal cycling between -125°C and +85°C, by a research collaborator. Based on the failure data, 7 different configurations were ranked, with 1 having the worst durability, as shown in Table 4.3. The failure ranking was based on a ‘severity metric’. The ‘severity metric’ was based on one of the three criteria below, in descending order of priority.

N_{100} – Number of cycles reached before 100% failure

P_{1500} - % failed at 1500 cycles

$N_{1st\ failure}$ – Number of cycles at first failure

Table 4.3 Thermal cycling test results [APL, 2005]

Sub.	Die Attach	Encap.	No. of Cycles Reached	% failed	Cycles at first failure	Rank
PI	ZVR 6000.2	FP 4402	1500	25	850	7
	TC-601.1	FP 4450	1500	50	150	5
Al2O3	ZVR 6000.2	FP 4402	1450	100	450	4
		FP 4450	300	100	150	2
	TC-601.1	FP 4402	150	100	50	1
	Ablebond 967-1	FP 4402	850	100	50	3
LTCC	ZVR 6000.2	FP 4450	1500	25	100	6

The test data shows that thermal fatigue durability is least in CoB assemblies that use Ceramic as the substrate material. To explore correlations between the severity metric estimated from the test data and the elastic strains predicted by the RR and FEA models, the test configurations provided in Table 4.3 were modeled. The material properties of the different materials were obtained from the literature [APL, 2005]. The geometric

parameters, held constant in the model, had the following values: (i) span: 56 mils, (ii) die thickness: 25 mils, (iii) die attach thickness: 1.5 mils and (iv) substrate thickness: 32 mils.

The correlation plot, presented in Figure 4.14, shows an overall monotonically decreasing trend, thus confirming that the elastic strains predicted by the model are a reasonably good indicator of the relative fatigue damage accumulation rates in each configuration, due to thermal cycling.

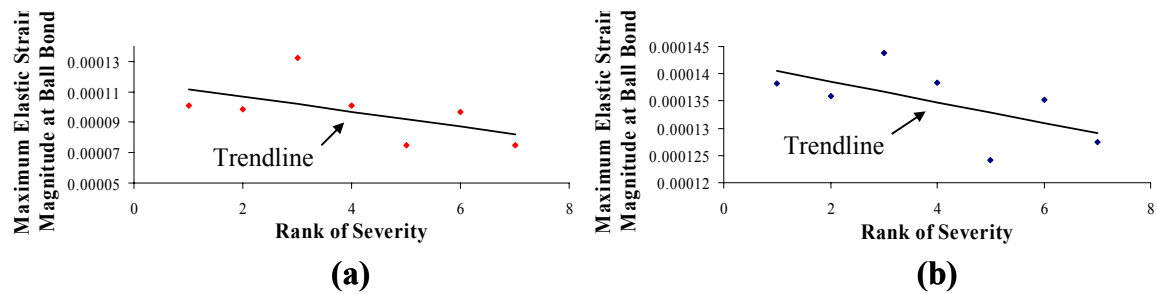


Figure 4.14 Comparison of the fatigue test results [APL, 2005] with (a) the RR model and (b) FEA

Although the observed failure trend has an overall correlation with the RR model and the FEA model estimates of elastic strains, the scatter in the plot is fairly large. This could be resulting from:

- the fact that material plasticity is not considered in this analysis,
- uncertainties in input material properties and geometry,
- possible manufacturing defects,
- geometric approximations in the model (eg. the use of only two cubic splines to represent a complex geometry),
- approximations in the assumed displacement field,

- model simplifications such as the use of straight beam theory to estimate bending energy in the wire
- and the RR model does not account for the out of plane effect of encapsulant shrinkage on the wire bond strain.

5 Conclusions, Contributions and Suggestions for Future Work

The conclusions, major accomplishments and contributions of this thesis are summarized in this chapter, along with suggestions for future work.

5.1 Conclusions

A simple 2-D Raleigh-Ritz (RR) elastic model has been developed to predict the strains in a ball-wedge wire configuration for encapsulated CoB packages. The initial wire profile is obtained by minimizing the strain energy of the wire. Plastic deformations are ignored in this study. This model is therefore suitable for parametric sensitivity studies to minimize wire stress by design, and is a starting point for subsequent plastic analysis and durability modeling. Parametric studies are conducted using the minimum energy wire profile model and the elastic RR model to assess the effects of design parameters and material properties used in the CoB package. The following are the key conclusions from this study:

- Large curvatures are observed at the ball bond, at points close to the maximum height in the wire loop, and at the wedge bond, indicating that these could be potential failure sites in unencapsulated wire bonds.
- Loop height for the wire profiles with the minimum strain energy is approximately 25% of the wire span.
- As shown in Figure 4.1, in order to minimize the elastic strain energy, the wire length must increase as the span increases (for a given die height). This results in higher electrical parasitics and Au wire cost.

- The RR model developed in this study has a well-defined range of validity for parametric design trade-off studies for various CoB Ball-Wedge wire bond configurations ($E_{\text{encap}} \geq 3$ GPa, wire dia ≤ 2 mils).
- The maximum elastic strains predicted by the RR model agree well with those predicted by more detailed FEA, within the range of validity of the model.
- The maximum elastic strain is at the ball bond, and increases with increase in die height, decreases with increase in span, and increases with increase in CTE of the encapsulant.
- The failure trend of samples provided in the test data has an overall correlation with the RR and FEA model estimates of elastic strains.

5.2 Contributions

The major accomplishments and contributions of this thesis are listed as follows:

- The first semi-analytic 2D model to estimate the minimum-energy profile for ball-wedge bond wires. The model is based on three critical geometric variables: the length of the wire, the Span (D) and the offset Height (H). If any two of these variables are specified, the model predicts the lowest-energy wire profile and the corresponding value for the third variable. The determination of wire profiles is critical both for finite element stress analysis as well as for damage and durability modeling based on physics of failure.
- The first semi-analytic 2D model to predict the elastic thermomechanical strains in a ball-wedge bond wire in an encapsulated microcircuit, based on the geometry and elastic material properties of the assembly. The model was compared against detailed FEA models for several different configurations.

- Parametric insights into the influence of package geometry and materials, on the wire bond profile prior to encapsulation, based on parametric studies using the RR model.
- Parametric insights into the influence of package geometry and materials on the elastic thermomechanical strains at the ball bond, in encapsulated wire bonds, based on parametric finite element and RR modeling.
- Insights into correlations between thermal cycling durability test results and the elastic strains predicted by FEA and RR models.

5.3 Limitations of the Existing Model

Even though the RR model agrees qualitatively with the FEA and the test results, there are limitations associated with the usage of the model for parametric analyses. The limitations are,

- The RR model can not be used for absolute prediction of profile or stress or strain or durability. The model is suited only for trade-off studies and parametric sensitivity studies, since plastic deformations have been ignored.
- The model is useful for predicting strains at the ball bond and at the peak of the wire loop only.
- The RR model cannot be used to predict strains in encapsulated CoB configurations which have bond wires of diameter less than 2 mils, or encapsulants of stiffness less than 3 GPa.

5.4 Suggestions for Future Work

Some of the suggestions for future work have been described as follows:

- The minimum energy wire profile model needs to include three or more cubic splines to obtain optimal wire geometry for shaped bond wires, and to capture positive curvature at the ball bond for some geometries, during thermal loading.

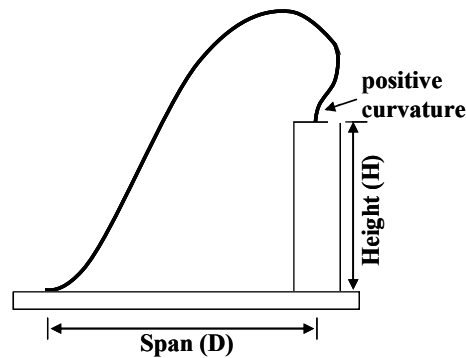


Figure 5.1 Ball-Wedge wire profile under thermal loading

- The model uses straight beam theory to calculate the bending energy in the wire. More research is required to investigate the usage of curved beam theory to calculate the bending energy in the wire.
- Since the model assumes only elastic deformation, further research needs to be done to include the effects of plastic deformations in the wire and the encapsulant.
- The RR model can be improved so that errors can be minimized for very compliant encapsulants and thicker bond wires, and near the wedge bond by improving the trial functions to account for detailed displacement gradients around the wire in the encapsulant.
- Further research is needed to understand how to improve the correlations between the experimental temperature cycling fatigue measurements, and trends predicted by the RR model and detailed FEA models.

- The current model is a 2D local model, which does not account for the out of plane effect of encapsulant shrinkage on the wire bond strain. A global model is needed to study this effect.
- Future work is needed to verify the RR and the FEA displacement fields using experimental techniques like Moiré interferometry.

$$u_I = u_{1sub} \left(\frac{x}{D} \right) + A \left[1 - e^{-a \left(\frac{y}{H} \right)} \right] \left(\frac{x-D}{D} \right) \quad (\text{A.1})$$

$$u_{II} = u_{1sub} + (u_{2sub} + u_{die}) \left(\frac{x-D}{L} \right) + B \left[1 - e^{-b \left(\frac{y-H}{H} \right)} \right] \left(\frac{x-(D+L)}{L} \right) \quad (\text{A.2})$$

$$u_{III} = u_{1sub} \left(\frac{x}{D} \right) + A \left[1 - e^{-a \left(\frac{y}{H} \right)} \right] \left(\frac{x-D}{D} \right) - B \left[1 - e^{-b \left(\frac{y-H}{H} \right)} \right] \left(\frac{x}{D} \right) \quad (\text{A.3})$$

‘a’ and ‘b’ in the Eqns A.1 – A.3 are constants fixed by using FE analysis. The method used in determining these constants is described in this section.

‘a’ appears in the displacement equations A.1 and A.2 (u_I and u_{II}). ‘a’ determines the variation of u from $y=0$ to $y=$ ‘encapsulant height’ in domains I and III. The schematic of the deformed CoB is shown in Figure A 2.

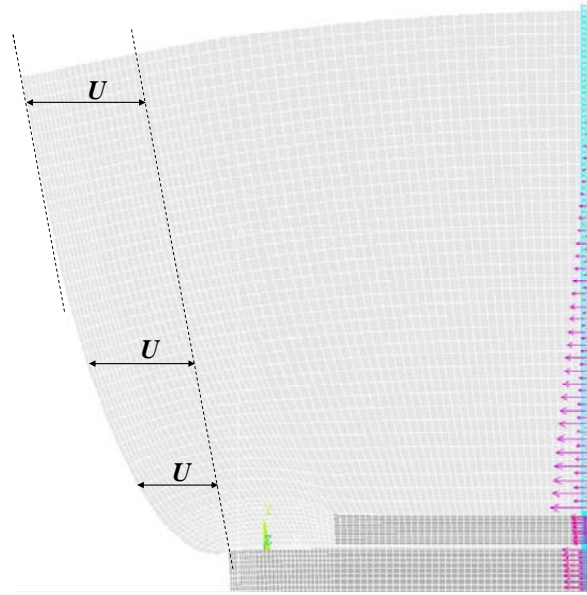


Figure A 2 Schematic of the Deformed CoB showing displacement in x-direction

The height of the encapsulant is chosen as ten times the height of the Si die. At this height the displacement in the x-direction tends to be constant. The dashed line passing through (0,0) is parallel to the tangent at (0,10H). ‘U’ describes the displacement

of the encapsulant in x-direction at x=0, and is equal to $B \left[1 - e^{-b \left(\frac{y-H}{H} \right)} \right]$ in domains I and

III. A is the CTE of the encapsulant which is 300 ppm/°C in this analysis. The values of U are obtained from FEA for CoB configurations with four different encapsulants. Only the Young's Modulus (E) of the encapsulant is varied in the four configurations (5, 10 15 and 20 GPa). 'a' is then obtained for each CoB by numerically minimizing the sum of

squares of difference between U and $A \left[1 - e^{-a \left(\frac{y}{H} \right)} \right]$,

$$\left(U - A \left[1 - e^{-a \left(\frac{y}{H} \right)} \right] \right)^2 \rightarrow 0 \quad (\text{A.4})$$

Once the values of 'a' for the four CoBs are obtained, a second order polynomial is fit using the Young's Moduli of the encapsulant used in the analysis. Thus, 'a' is given as

$$a = 4.0449 \left(10^{-9} \right) E_{\text{encapsulant}}^2 - 8.5807 \left(10^{-5} \right) E_{\text{encapsulant}} + 3.3374 \quad (\text{A.5})$$

Determination of 'b':

'b' appears in the displacement equations A.2 and A.3 (u_{II} and u_{III}). 'b' determines the variation of u from $y=H$ to $y=$ 'encapsulant height' in domains II and III. The displacements in x-directions at ($x=D$, $y=$ 'loop height $\sim H+0.25D$ ') and ($x=D$, $y=10H$) are obtained from FEA. The ratios of $U_{(D,H+0.25D)}$ to $U_{(D,10H)}$ for the four different CoB configurations is written as a quadratic polynomial in Young's Modulus (E) of the encapsulant. Also, the ratio is approximated as follows,

$$\frac{U_{(D,H+0.25D)}}{U_{(D,10H)}} \Rightarrow f(E) \cong 1 - e^{-b \left(\frac{y-H}{H} \right)} @ y = H + 0.25D \quad (\text{A.6})$$

where, $f(E) = -2 \left(10^{-11} \right) E_{\text{encapsulant}}^2 + 4 \left(10^{-6} \right) E_{\text{encapsulant}} + 0.168$

Equation A.6 results in a function that gives the value of b, which is given by,

$$b = -\frac{4H}{D} \ln[1 - f(E)] \quad (\text{A.7})$$

Determination of ‘g’:

The displacement fields in y-direction chosen for the analysis are:

$$v_I = (v_{die} + v_{dieattach}) e^{k_1 + \frac{k_2}{H} \left(\frac{y}{H}\right)} + G \left[1 - e^{-g \left(\frac{D-x}{D}\right)} \right] \left(\frac{y}{H}\right) \quad (\text{A.8})$$

$$v_{II} = \left[v_{die} + v_{dieattach} + K \left(\frac{y-H}{H}\right) \right] e^{k_1 \left(\frac{D+L-x}{L}\right) + k_2 \left(\frac{1}{y}\right)} \quad (\text{A.9})$$

$$v_{III} = (v_{die} + v_{dieattach}) e^{k_1 + \frac{k_2}{y}} + K \left(\frac{y-H}{H}\right) e^{k_1 + \left(\frac{k_2}{y}\right)} + G \left[1 - e^{-g \left(\frac{D-x}{D}\right)} \right] \left(\frac{H}{y}\right) \quad (\text{A.10})$$

‘g’, ‘k₁’ and ‘k₂’ in the above equations are constants fixed by using FE analysis. The method used in determining these constants is described in this section.

‘g’ appears in the displacement equations A.8 and A.10 (v_I and v_{III}). ‘g’ determines the variation of v from $x=0$ to $x=D$ in domains I and III. The schematic of the deformed CoB is shown in Figure A 3.

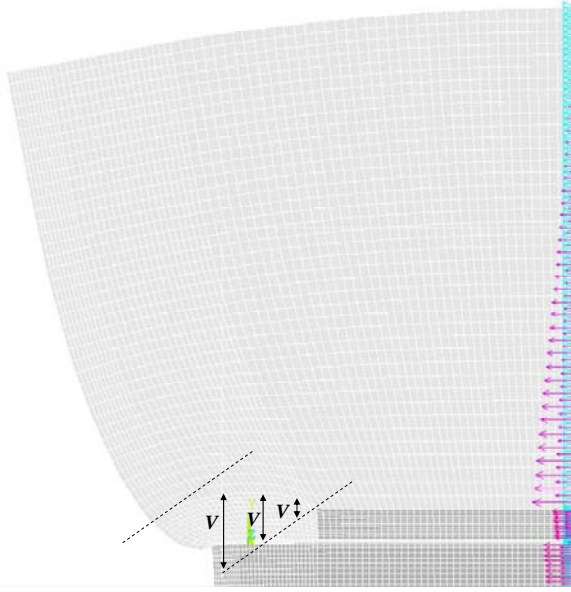


Figure A 3 Schematic of the Deformed CoB showing displacement in y-direction

The height of the encapsulant is chosen as ten times the height of the Si die. At this height the displacement in the y-direction tends to be constant. The dashed line passing through (D, H) is parallel to the tangent at $(0, H)$. ‘ V ’ describes the displacement

of the encapsulant in y-direction at $y=H$, and is equal to $G \left[1 - e^{-g \left(\frac{D-x}{D} \right)} \right]$ in domains I and

III. G is the CTE of the encapsulant which is $300 \text{ ppm}/^\circ\text{C}$ in this analysis. The values of V are obtained from FEA for CoB configurations with four different encapsulants. Only the Young’s Modulus (E) of the encapsulant is varied in the four configurations (5, 10 15 and 20 GPa). ‘ g ’ is then obtained for each CoB by numerically minimizing the sum of squares

of difference between V and $G \left[1 - e^{-g \left(\frac{D-x}{D} \right)} \right]$,

$$\left(V - G \left[1 - e^{-g \left(\frac{D-x}{D} \right)} \right] \right)^2 \rightarrow 0 \quad (\text{A.11})$$

Once the values of ‘g’ for the four CoBs are obtained, a second order polynomial is fit using the Young’s Modulii of the encapsulant used in the analysis. Thus, ‘g’ is given as

$$g = 1.6309(10^{-9})E_{encapsulant}^2 - 1.4923(10^{-4})E_{encapsulant} + 6.4482 \quad (\text{A.12})$$

Determination of ‘k₁’:

‘k₁’ determines the variation of ν from $x=D$ to $x=D+L$ in domains II. The displacements in y-directions at ($x=D$, $y=\text{loop height} \sim H+0.25D$) and ($x=D+L$, $y=\text{loop height} \sim H+0.25D$) are obtained from FEA. The ratios of $V_{(D,H+0.25D)}$ to $V_{(D+L,H+0.25D)}$ for the four different CoB configurations is written as a quadratic polynomial in Young’s Modulus (E) of the encapsulant. Also, the ratio is approximated as follows,

$$\frac{V_{(D,H+0.25D)}}{V_{(D+L,H+0.25D)}} \Rightarrow f(E) \cong e^{-k_1 \left(\frac{D+L-x}{L} \right)} @ x = D \quad (\text{A.13})$$

where, $f(E) = -5(10^{-11})E_{encapsulant}^2 + 3(10^{-6})E_{encapsulant} + 1.0081$

Equation A.13 results in a function that gives the value of k_1 , which is given by,

$$k_1 = \ln[f(E)] \quad (\text{A.14})$$

Determination of ‘k₂’:

‘k₂’=0.05 and was obtained by parametrically changing its value, keeping the already obtained values of a, b, g and k₁, to minimize the error between the assumed displacement functions in x and y directions with FEA.

Appendix B

The strain energies in the encapsulant and in the wire due to bending and stretching under a thermal load are shown in Eqns B.1 – B.3.

$$U_{encap} = \frac{1}{2} \int_{\Omega_1} (\varepsilon_{total} - \varepsilon_{thencap})^T \cdot C_{encap} \cdot (\varepsilon_{total} - \varepsilon_{thencap}) dV \quad (B.1)$$

$$U_{bend} = \frac{1}{2} \int_0^L E_{wire} I_{wire} \left(\frac{\partial^2 V_n}{\partial s^2} \right)^2 ds \quad (B.2)$$

$$U_{stretch} = \frac{1}{2} \int_0^L E_{wire} A_{wire} (\varepsilon_{ss} - \varepsilon_{thwire})^2 ds \quad (B.3)$$

Domain III – Curve 1

For domain III and curve 1, Equation B.2 results in the following expression,

$$U_{bend_{1c}} = \frac{1}{2} \int_0^{l_{1c}} E_{wire} I_{wire} \left(\frac{\partial^2 V_{n_{1c}}}{\partial s_{1c}^2} \right)^2 ds_{1c} \quad (B.4)$$

where, l_{1c} is the length of the wire in domain III and is equal to parameter u for $y_1(u) > H$.

In the subscript ‘1c’, ‘1’ represents the first cubic spline and ‘c’ represents the domain III.

Furthermore, Eq. B.4 also accounts for the respective displacement fields, u_{III} and v_{III} .

Therefore, in the parametric form,

$$\begin{aligned} \frac{\partial^2 V_{n_{1c}}}{\partial s_{1c}^2} &= \frac{\partial}{\partial s_{1c}} \left(\frac{\partial V_{n_{1c}}}{\partial s_{1c}} \right) = \frac{d}{du} \left(\frac{\partial V_{n_{1c}}}{\partial s_{1c}} \right) \frac{du}{ds_{1c}} = \frac{d}{du} \left(\frac{dV_{n_{1c}}}{du} \frac{du}{ds_{1c}} \right) \frac{du}{ds_{1c}} \\ V_{n_{1c}} &= -u_{1c} \sin \theta_{1c} + v_{1c} \cos \theta_{1c} = -u_{1c} \left(\frac{dy_{1c}}{ds_{1c}} \right) + v_{1c} \left(\frac{dx_{1c}}{ds_{1c}} \right) \\ &= -u_{1c} \left(\frac{dy_{1c}}{du} \frac{du}{ds_{1c}} \right) + v_{1c} \left(\frac{dx_{1c}}{du} \frac{du}{ds_{1c}} \right) \end{aligned} \quad (B.5)$$

where, $ds_{1c} = \sqrt{(dx_{1c})^2 + (dy_{1c})^2} du$, u_{1c} is u_{III} , v_{1c} is v_{III} , x_{1c} is x_1 and y_{1c} is y_1 .

In Eq. B.3, ε_{ss} in domain III for curve 1 can be parametrically shown as,

$$\begin{aligned}
\varepsilon_{ss_{1c}} &= \varepsilon_{xx_{1c}} \text{Cos}^2\theta_{1c} + \varepsilon_{yy_{1c}} \text{Sin}^2\theta_{1c} + \gamma_{xy_{1c}} \text{Sin}\theta_{1c} \text{Cos}\theta_{1c} \\
&= \frac{\partial u_{1c}}{\partial x_{1c}} \left(\frac{\partial x_{1c}}{\partial s_{1c}} \right)^2 + \frac{\partial v_{1c}}{\partial y_{1c}} \left(\frac{\partial y_{1c}}{\partial s_{1c}} \right)^2 + \left(\frac{\partial u_{1c}}{\partial y_{1c}} + \frac{\partial v_{1c}}{\partial x_{1c}} \right) \left(\frac{\partial y_{1c}}{\partial s_{1c}} \right) \left(\frac{\partial x_{1c}}{\partial s_{1c}} \right) \\
&= \left(\frac{du_{1c}}{du} \frac{du}{dx_{1c}} \right) \left(\frac{dx_{1c}}{du} \frac{du}{ds_{1c}} \right)^2 + \left(\frac{dv_{1c}}{du} \frac{du}{dy_{1c}} \right) \left(\frac{dy_{1c}}{du} \frac{du}{ds_{1c}} \right)^2 + \\
&\quad \left(\frac{du_{1c}}{du} \frac{du}{dy_{1c}} + \frac{dv_{1c}}{du} \frac{du}{dx_{1c}} \right) \left(\frac{dy_{1c}}{du} \frac{du}{ds_{1c}} \right) \left(\frac{dx_{1c}}{du} \frac{du}{ds_{1c}} \right)
\end{aligned} \tag{B.6}$$

Domain III – Curve 2

For domain III and curve 2, Equation B.2 results in the following expression,

$$U_{bend_{2c}} = \frac{1}{2} \int_0^{l_{2c}} E_{wire} I_{wire} \left(\frac{\partial^2 V_{n_{2c}}}{\partial s_{2c}^2} \right)^2 ds_{2c} \tag{B.7}$$

where, l_{1c} is the length of the wire in domain III and is equal to parameter u for $y_1(u) > H$.

In the subscript ‘1c’, ‘1’ represents the first cubic spline and ‘c’ represents the domain III.

Furthermore, Eq. B.7 also accounts for the respective displacement fields, u_{III} and v_{III} .

Therefore, in the parametric form,

$$\begin{aligned}
\frac{\partial^2 V_{n_{2c}}}{\partial s_{2c}^2} &= \frac{\partial}{\partial s_{2c}} \left(\frac{\partial V_{n_{2c}}}{\partial s_{2c}} \right) = \frac{d}{du} \left(\frac{\partial V_{n_{2c}}}{\partial s_{2c}} \right) \frac{du}{ds_{2c}} = \frac{d}{du} \left(\frac{dV_{n_{2c}}}{du} \frac{du}{ds_{2c}} \right) \frac{du}{ds_{2c}} \\
V_{n_{2c}} &= -u_{2c} \text{Sin}\theta_{2c} + v_{2c} \text{Cos}\theta_{2c} = -u_{2c} \left(\frac{\partial y_{2c}}{\partial s_{2c}} \right) + v_{2c} \left(\frac{\partial x_{2c}}{\partial s_{2c}} \right) \\
&= -u_{2c} \left(\frac{dy_{2c}}{dv} \frac{dv}{ds_{2c}} \right) + v_{2c} \left(\frac{dx_{2c}}{dv} \frac{dv}{ds_{2c}} \right)
\end{aligned} \tag{B.8}$$

where, $ds_{2c} = \sqrt{(dx_{2c})^2 + (dy_{2c})^2} dv$, u_{2c} is u_{III} , v_{2c} is v_{III} , x_{2c} is x_2 and y_{2c} is y_2 .

In Eq. B.3, ε_{ss} in domain III for curve 2 can be parametrically shown as,

$$\begin{aligned}
\varepsilon_{ss_{2c}} &= \varepsilon_{xx_{2c}} \text{Cos}^2\theta_{2c} + \varepsilon_{yy_{2c}} \text{Sin}^2\theta_{2c} + \gamma_{xy_{2c}} \text{Sin}\theta_{2c} \text{Cos}\theta_{2c} \\
&= \frac{\partial u_{2c}}{\partial x_{2c}} \left(\frac{\partial x_{2c}}{\partial s_{2c}} \right)^2 + \frac{\partial v_{2c}}{\partial y_{2c}} \left(\frac{\partial y_{2c}}{\partial s_{2c}} \right)^2 + \left(\frac{\partial u_{2c}}{\partial y_{2c}} + \frac{\partial v_{2c}}{\partial x_{2c}} \right) \left(\frac{dy_{2c}}{ds_{2c}} \right) \left(\frac{dx_{2c}}{ds_{2c}} \right) \\
&= \left(\frac{du_{2c}}{dv} \frac{dv}{dx_{2c}} \right) \left(\frac{dx_{2c}}{dv} \frac{dv}{ds_{2c}} \right)^2 + \left(\frac{dv_{2c}}{dv} \frac{dv}{dy_{2c}} \right) \left(\frac{dy_{2c}}{dv} \frac{dv}{ds_{2c}} \right)^2 + \\
&\quad \left(\frac{du_{2c}}{dv} \frac{dv}{dy_{2c}} + \frac{dv_{2c}}{dv} \frac{dv}{dx_{2c}} \right) \left(\frac{dy_{2c}}{dv} \frac{dv}{ds_{2c}} \right) \left(\frac{dx_{2c}}{dv} \frac{dv}{ds_{2c}} \right)
\end{aligned} \tag{B.9}$$

Strain Energy of the Encapsulant

For domain II, $\varepsilon_{\text{total}}$ in Eq. B.1 can be represented as follows,

$$\varepsilon_{\text{total}_B} = \begin{bmatrix} \frac{\partial u_B}{\partial x_B} \\ \frac{\partial v_B}{\partial y_B} \\ \frac{\partial u_B}{\partial y_B} + \frac{\partial v_B}{\partial x_B} \end{bmatrix} \tag{B.10}$$

where, x_{II} represents $x = D$ to $x = D + L_{\text{die}}$, and y_{II} represents $y = H$ to $y = H_{\text{encap}}$.

Accordingly, for domain III $\varepsilon_{\text{total}}$ in Eq. B.1 can be represented as follows,

$$\varepsilon_{\text{total}_C} = \begin{bmatrix} \frac{\partial u_C}{\partial x_C} \\ \frac{\partial v_C}{\partial y_C} \\ \frac{\partial u_C}{\partial y_C} + \frac{\partial v_C}{\partial x_C} \end{bmatrix} \tag{B.11}$$

where, x_{III} represents $x = 0$ to $x = D$, and y_{III} represents $y = H$ to $y = H_{\text{encap}}$.

Appendix C

Minimization of the potential energy (Π) with respect to all the parameters in the trial functions, results in values for these adjustable coefficients. Let the unknown coefficients form the vector of degrees of freedom, \vec{X} .

$$X = [A \quad B \quad u_{1sub} \quad u_{2sub} \quad u_{die} \quad v_{die} \quad v_{dieattach} \quad K \quad G] \quad (C.1)$$

Thus energy minimization leads to the stationary condition:

$$\frac{\partial \Pi}{\partial X_i} = 0 \quad i = 1 - 9 \quad (C.2)$$

This leads to 9 linear, simultaneous equations in 9 unknowns, and can be solved using standard linear algebra techniques. To verify whether the energy minimization leads to a stationary condition, the strain energy was plotted against each parameter, X_i , and checked for global minimum. The following are the values used in this analysis.

$$\begin{aligned} A &= -0.0000224319 \\ B &= -0.0000112798 \\ u_{1sub} &= -0.000103839 \\ u_{2sub} &= -0.000192242 \\ u_{die} &= -0.0000867698 \\ v_{die} &= -5.10884 \cdot 10^{-6} \\ v_{dieattach} &= -0.0000208555 \\ K &= -0.0000763029 \\ G &= -0.0000335419 \end{aligned}$$

$$\begin{aligned} \alpha_{encapsulant} &= 100 \text{ ppm/}^\circ\text{C} \\ E_{encapsulant} &= 10 \text{ GPa} \\ \nu_{encapsulant} &= 0.4 \\ \alpha_{dieattach} &= 156 \text{ ppm/}^\circ\text{C} \\ E_{dieattach} &= 1.6 \text{ GPa} \\ \nu_{dieattach} &= 0.4 \\ \alpha_{substrate} &= 59 \text{ ppm/}^\circ\text{C} \\ E_{substrate} &= 16.5 \text{ GPa} \\ \alpha_{die} &= 2.6 \text{ ppm/}^\circ\text{C} \\ E_{die} &= 115 \text{ GPa} \end{aligned}$$

diameter of the bond wire = 1 mil;
 $\alpha_{\text{wire}} = 14.2 \text{ ppm}/^\circ\text{C}$
 $E_{\text{wire}} = 78 \text{ GPa}$

Span = 50 mils
Die Thickness = 25 mils
Die Attach Thickness = 1.5 mils
 $d = 46.4022 \text{ mils}$
 $h = 34.3590 \text{ mils}$
Die size = 5 mm
Bond pitch = 10 mils
Substrate thickness = 62 mils
 $dT = -1^\circ\text{C}$

One of the 9 parameters was varied at a time while keeping the rest constant. Each strain energy plot obtained has a global minimum for each parameter.

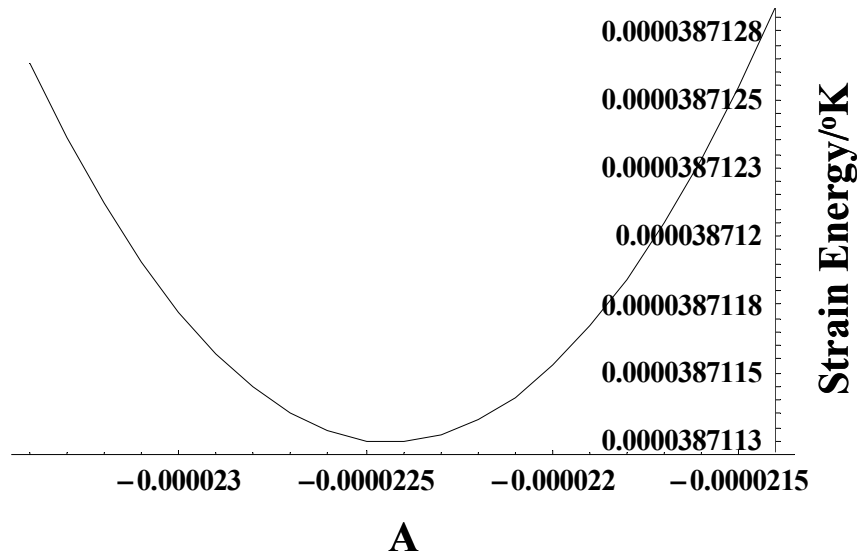


Figure C 1 Plot of Strain Energy vs. A

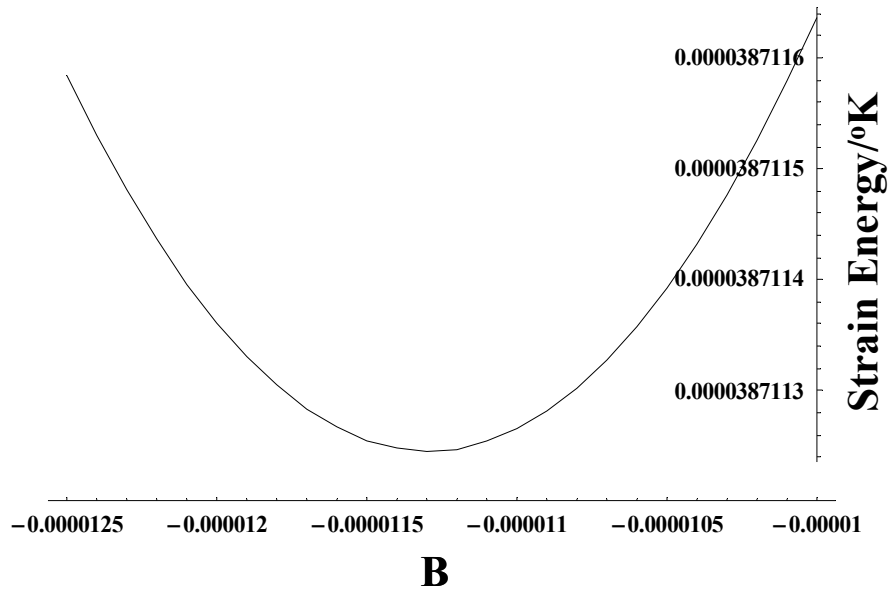


Figure C 2 Plot of Strain Energy vs. B

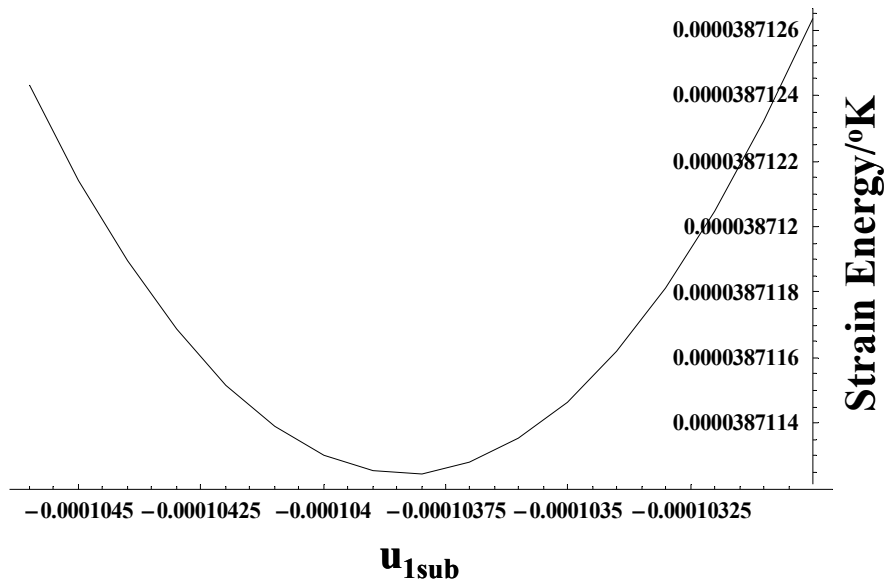


Figure C 3 Plot of Strain Energy vs. C

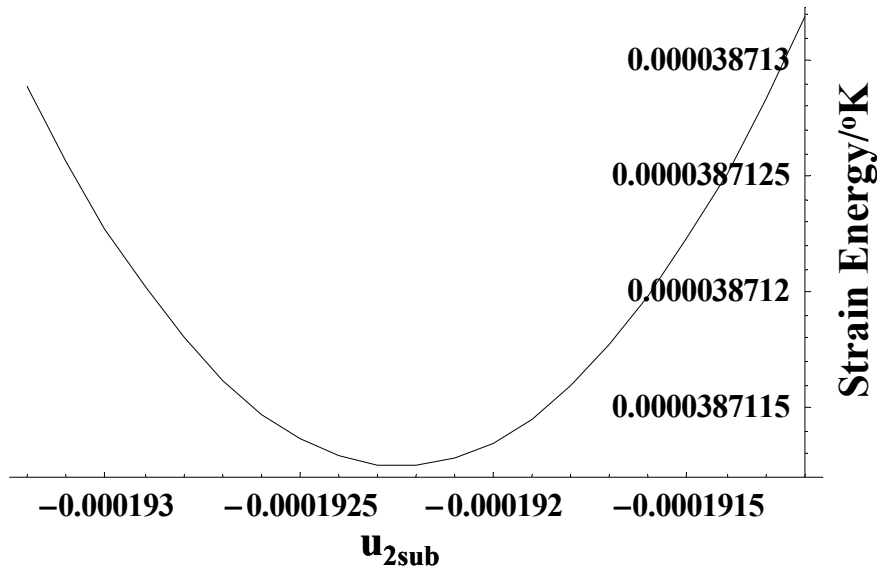


Figure C 4 Plot of Strain Energy vs. u_{2sub}

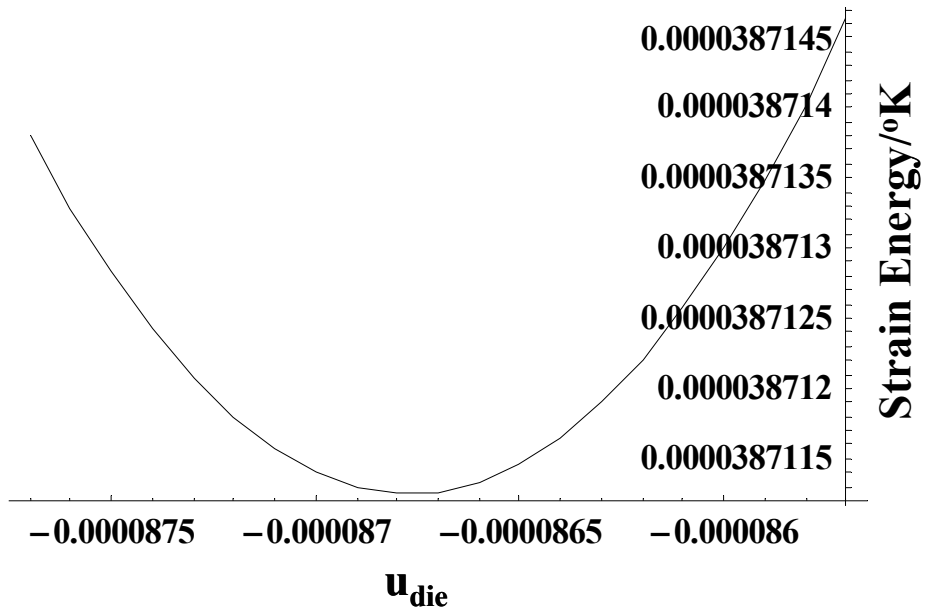


Figure C 5 Plot of Strain Energy vs. u_{die}

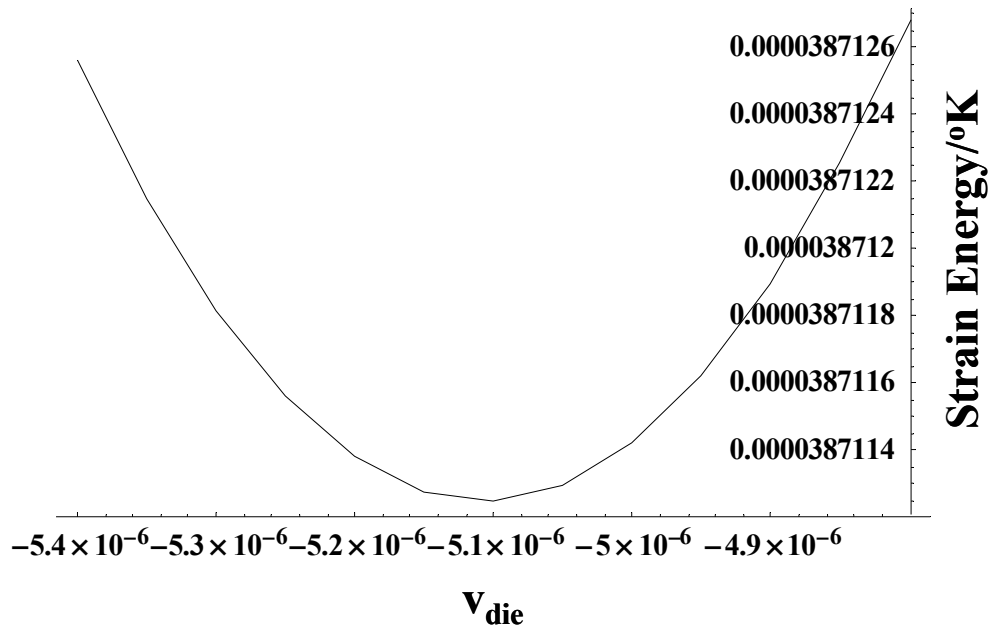


Figure C 6 Plot of Strain Energy vs. V_{die}

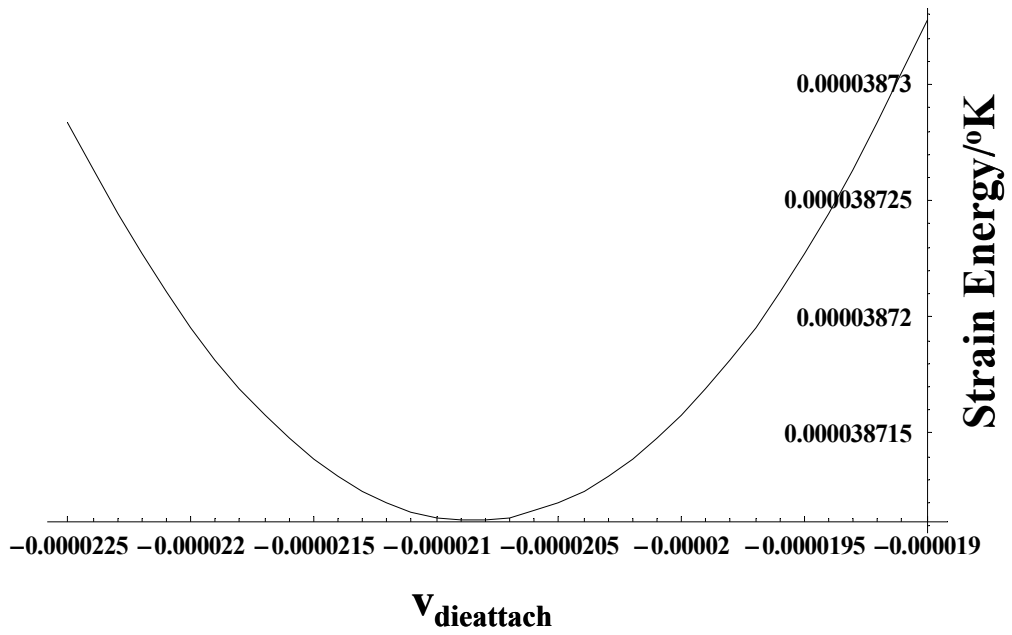


Figure C 7 Plot of Strain Energy vs. $V_{dieattach}$

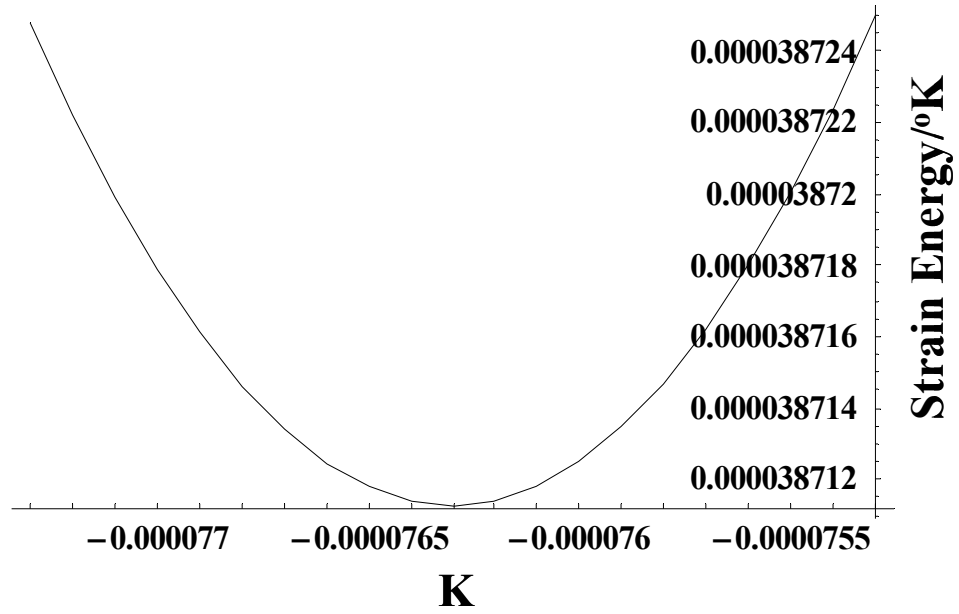


Figure C 8 Plot of Strain Energy vs. K

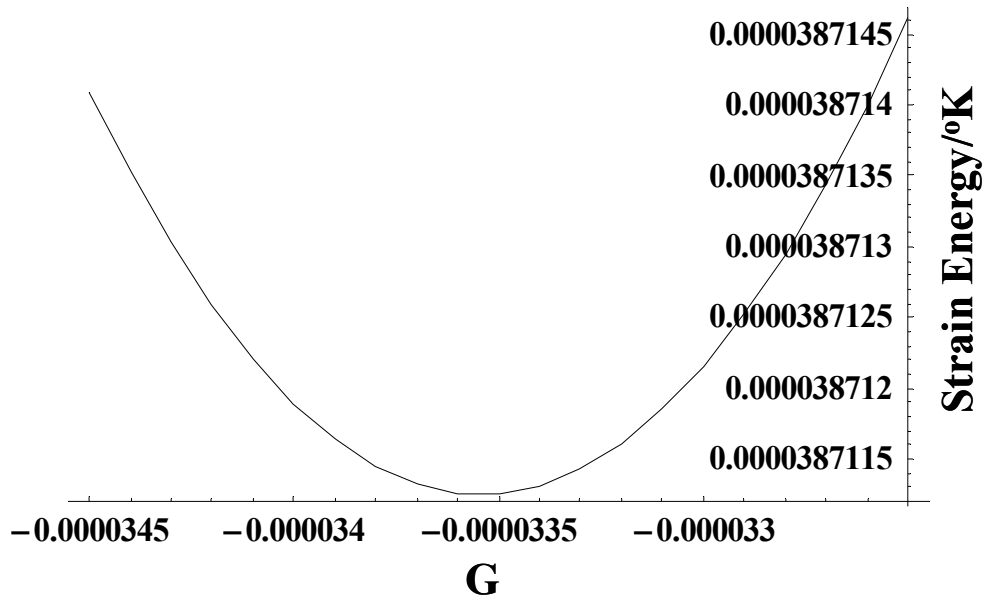


Figure C 9 Plot of Strain Energy vs. G

Appendix D

The mathematical tools used for the analysis are MATLAB and MATHEMATICA. Matlab is used primarily to obtain the optimal ball wedge wire profile before encapsulation. It also is used to calculate the length of the wire. The code developed for carrying out the aforementioned tasks is given below. The sentences starting with ‘%’ are comments while coding in Matlab.

```
% The following code is used to get the optimal wire profile for the given values of span
% (D) and height offset (H), which is the sum of die thickness and die attach thickness. It
% also calculates the total wire length for the optimal profile.
H
D
temp=[D H];
length=0;
d1=D-(0.09*D);
h1=H+(0.2*D);
p0=[d1
    h1];
% The inbuilt MATLAB function ‘fminsearch’ passes D and H to ‘spline’ and minimizes
% the bending strain energy for ‘d’ and ‘h’ to get optimal wire profile, and returns d and
h to m.
m=fminsearch(@spline,p0,[],temp);
d=m(1);
h=m(2);
u=0:0.0001:1;
x1=u.*d;
y1=u.*h-((u.*h).*(1-u).^2)-(d*y3-h)*(1-u).*u.^2;
v=0:0.0001:1;
x2=((1-v).*d)+(v.*D)+((D-d)*(1-v).*v.^2);
y2=(1-v).*h + (v.*H) + (((D-d)*y3-(H-h))*v.*(1-v.*2+v.^2));
plot(x1,y1,x2,y2) % plots
axis equal
a=d*(D-d)/((2*D)+d);
b=2*(H-h)/((D-d)^2);
c=3*h/(d^2);
y3=a*(b+c);
% The inbuilt MATLAB function ‘quadl’ is used to numerically integrate a function.
‘length1’ and ‘length2’ are functions that are used to calculate the length of curve 1 and
curve 2 respectively.
wirelength = quadl(@length1,0,1,[],[],d,h,y3) + quadl(@length2,0,1,[],[],d,h,y3,D,H);
```

```

% Calculation of bending energy in the wire
function energy=spline(p0,temp)
d=p0(1);
h=p0(2);
D=temp(1);
H=temp(2);
a=d*(D-d)/((2*D)+d);
b=2*(H-h)/((D-d)^2);
c=3*h/(d^2);
y3=a*(b+c);
% 'myfun1' and 'myfun2' are integrals of the bending strain energies in curve 1 and
curve 2, respectively.
energy = quadl(@myfun1,0,1,[],[],d,h,y3)) + (quadl(@myfun2,0,1,[],[],d,h,y3,D,H);

```

```

% The following function integrates the strain energy in curve 1 and returns the value to
% 'spline'

```

```

function c=myfun1(ut,d,h,y3)
u=ut;
d=d;
h=h;
y3=y3;
y1p = (h*(4*u-3*u.^2) - ((y3*d-h)*(2*u-3*u.^2)))/d;
y1dp = (h*(4-6*u) - ((y3*d-h)*(2-6*u)))/(d^2);
c = d * ((y1dp).^2) ./ ((1 + (y1p).^2).^2.5);

```

```

% The following function integrates the strain energy in curve 2 and returns the value to
% the function 'spline'

```

```

function c=myfun2(vt,d,h,y3,D,H)
v=vt;
d=d;
h=h;
H=H;
D=D;
y3=y3;
D1=(D-d);
v1 = (1+2*v-(3*(v.^2)));
v2 = ((3*(v.^2))-4*v+1);
H1=(H-h);
y2pv = H1 + (((D1*y3)-H1)*v2);
x2pv = D1 * v1;
k = ((x2pv.*(6*v-4).*((D1*y3)-H1)) - (y2pv.*(2-6*v).* D1))./((x2pv.^2 +
y2pv.^2).^1.5);
ds2 = (x2pv.^2 + y2pv.^2).^0.5);
c = (k.^2).*ds2;

```

% The following function integrates the differential length in curve 1 and returns the
 % value of total length of curve 1 to 'wirelength'

```
function len=length1(ut,d,h,y3)
u=ut;
d=d;
h=h;
y3=y3;
y1p = (h*(4*u-3*u.^2) - ((y3*d-h)*(2*u-3*u.^2)))/d;
len = d * ((1 + (y1p).^2).^0.5);
```

% The following function integrates the differential length in curve 2 and returns the
 % value of total length of curve 1 to 'wirelength'

```
function len=length2(vt,d,h,y3,D,H)
v=vt;
d=d;
h=h;
H=H;
D=D;
y3=y3;
D1=(D-d);
v1 = (1+2*v-(3*v.^2));
v2 = ((3*v.^2)-4*v+1);
H1=(H-h);
y2pv = H1 + (((D1*y3)-H1)*v2);
x2pv = D1 * v1;
ds2 = (x2pv.^2 + y2pv.^2).^0.5;
len = ds2;
```

MATHEMATICA is primarily used to calculate the thermo-mechanical strains in the ball wedge bond wire along the wire profile in an encapsulated CoB. The following Mathematica code takes initial wire profile obtained from the MATLAB code, and the material properties as input values and calculates the strains. The sentences between (* and *) are comments. The units used for the values are in mm unless mentioned otherwise.

```
ClearAll[]
Off[General::spell1]
Off[General::spell]
```

```

(* Input the material properties for ENCAPSULANT *)
Encapalpha (* CTE of encapsulant material, units: ppm/°C*)
Eencap (* Young's Modulus of encapsulant material, units: N/mm^2 *)
nuencap (* Poisson's Ratio of encapsulant material *)
(* DIE ATTACH *)
daalpha (* CTE of die attach material, units: ppm/°C*)
Edieattach (* Young's Modulus of die attach material, units: N/mm^2 *)
(* SUBSTRATE *)
subalpha (* CTE of substrate or PWB material, units: ppm/°C*)
Esub (* Young's Modulus of substrate or PWB material, units: N/mm^2 *)
(* SILICON DIE *)
diealpha (* CTE of Silicon die, units: ppm/°C*)
Edie (* Young's Modulus of Silicon die, units: N/mm^2 *)
(* GOLD WIRE *)
dia (* diameter of the wire *)
alphawire (* CTE of bond wire, units: ppm/°C*)
Ewire (* Young's Modulus of bond wire, units: N/mm^2 *)
S (* Span *)
Hdie (* thickness of the die *)
Hda (* thickness of die attach *)
d (* d obtained from Matlab code *)
h (* h obtained from Matlab code *)
H = Hdie + Hda;
planethk (* ball bond pitch *)
a1 = d*(S - d)/((2*S) + d);
b1 = 2*(H - h)/((S - d)^2);
c1 = 3*h/(d^2);
y3 = a1*(b1 + c1);
u = Table[i, {i, 0, 1, 0.0001}];
x1 = u*d;
y1 = u*h - ((u*h)*(1 - u)^2) - (d*y3 - h)*(1 - u)*u^2;
ymax = Max[y1]
For[z = 1, z ≤ 10001, z++, If[y1[[z]] ≤ H, t = (z)/10000]]
t;
L (* half the size of the die *)
Sc = S + L;
Hc = (10/39.37) + ymax;
subthick (* thickness of the substrate or PWB *)
Clear[u];
radius = dia/2;
Ar = Pi*(dia^2)/4; (* cross sectional area of the bond wire *)
Iner = Pi*(dia^4)/64; (* moment of inertia of the bond wire about z-axis *)
dT = -1;
(* Plane Stress *)
stiff = {{1, nuencap, 0}, {nuencap, 1, 0}, {0, 0, ((1 - nuencap)/2)}};

```

```

SM = (Eencap/(1 - nuencap^2))*stiff;
ethencap = {encapalpha, encapsalpha, 0}*dT;
f2 = -2*10^(-11)*(Eencap^2) + 4*10^(-6)*Eencap + 0.168;
b = (-4*H/S)*Log[1 - f2]
f4 = -5*10^(-11)*(Eencap^2) + 3*10^(-6)*Eencap + 1.0081;
k1 = Log[f4]
k2 = 0.05;
a = 4.0449*(10^-009)*Eencap^2 + (-8.5807)*(10^-005)*Eencap + 3.3374;
g = 1.6309*(10^-009)*Eencap^2 + (-1.4923)*(10^-004)*Eencap + 6.4482;
ucterm = u1sub;
vcterm = vdie + vdieattach;
a1 = d*(S - d)/((2*S) + d);
b1 = 2*(H - h)/((S - d)^2);
c1 = 3*h/(d^2);
y3 = a1*(b1 + c1);

```

(* Uwire1underH calculates the strain energy of wire represented by curve 1 in domain A due to bending *)

```

x1a = u*d;
y1a = u*h - ((u*h)*(1 - u)^2) - (d*y3 - h)*(1 - u)*u^2;
ua = (ucterm/S)*(x1a) + A*(1 - Exp[-a*(y1a/H)])*((x1a - S)/S);
va = (vcterm/H)*(Exp[k1 + (k2/H)]*(y1a) + G*(1 - Exp[-g*((S - x1a)/S)]*(y1a/H));
y1apu = D[y1a, u];
x1apu = D[x1a, u];
y1adpu = D[y1apu, u];
x1adpu = D[x1apu, u];
uapu = D[ua, u];
vapu = D[va, u];
vadpu = D[vapu, u];
uadpu = D[uapu, u];
s1apu = (x1apu^2 + y1apu^2)^(0.5);(*differential length*)
duds1a = 1/s1apu;
costh1 = x1apu/s1apu;
sinth1 = y1apu/s1apu;
vna=-ua*sinth1+va*costh1;
dvnads=D[vna,u]*duds1a;
dvnadps = D[dvnads, u]*duds1a;
Uwire1underH = (1/2)*Ewire*Iner*((dvnadps)^2)*s1apu;

```

(* Uwire1overH calculates the strain energy of wire represented by curve 1 in domain C due to bending *)

```

x1c = u*d;
y1c = u*h - ((u*h)*(1 - u)^2) - (d*y3 - h)*(1 - u)*u^2;
uc1 = (ucterm/S)*(x1c) + A*(1 - Exp[-a*(y1c/H)])*((x1c - S)/S) - B*(1 - Exp[-b*((y1c - H)/H)]*(x1c/S);

```

```

vc1 = vcterm*(Exp[k1 + (k2/y1c)]) + G*(1 - Exp[-g*((S - x1c)/S)])*(H/y1c) + K*((y1c -
H)/H)*(Exp[k1 + (k2/y1c)]);
y1cpu = D[y1c, u];
x1cpu = D[x1c, u];
y1cdpu = D[y1cpu, u];
x1cdpu = D[x1cpu, u];
ucpu = D[uc1, u];
vcpu = D[vc1, u];
ucdpu = D[ucpu, u];
vcdpu = D[vcpu, u];
s1cpu = (x1cpu^2 + y1cpu^2)^(0.5);
duds1c = 1/s1cpu;
costh1 = x1cpu/s1cpu;
sinh1 = y1cpu/s1cpu;
vnc1=-uc1*sinh1+vc1*costh1;
dvncds=D[vnc1,u]*duds1c;
dvncdps = D[dvncds, u]*duds1c;
Uwire1overH = (1/2)*Ewire*Iner*((dvncdps)^2)*s1cpu;

```

(* Uwire2overH calculates the strain energy of wire represented by curve 2 in domain C due to bending *)

```

x2c = ((1 - v)*d) + (v*S) + ((S - d)*(1 - v)*v^2);
y2c = (1 - v)*h + (v*H) + (((S - d)*y3 - (H - h))*v*(1 - v^2 + v^2));
uc2 = (ucterm/S)*(x2c) + A*(1 - Exp[-a*(y2c/H)])*((x2c - S)/S) - B*(1 - Exp[-b*((y2c -
H)/H)])*(x2c/S);
vc2 = vcterm*(Exp[k1 + (k2/y2c)]) + G*(1 - Exp[-g*((S - x2c)/S)])*(H/y2c) + K*((y2c -
H)/H)*(Exp[k1 + (k2/y2c)]);
y2cpv = D[y2c, v];
x2cpv = D[x2c, v];
y2cdpv = D[y2cpv, v];
x2cdpv = D[x2cpv, v];
ucpv = D[uc2, v];
vcpv = D[vc2, v];
ucdpv = D[ucpv, v];
vcdpv = D[vcpv, v];
s2cpv = (x2cpv^2 + y2cpv^2)^(0.5);
dvds2c = 1/s2cpv;
costh2 = x2cpv/s2cpv;
sinh2 = y2cpv/s2cpv;
vnc2=-uc2*sinh2+vc2*costh2;
dvncds=D[vnc2,v]*dvds2c;
dvncdps = D[dvncds, v]*dvds2c;
Uwire2overH = (1/2)*Ewire*Iner*((dvncdps)^2)*s2cpv;

```

(* Umem1underH calculates the strain energy of wire represented by curve 1 in domain A due to stretch *)

```

Clear[x1a]
Clear[y1a]
ua = (ucterm/S)*(x1a) + A*(1 - Exp[-a*(y1a/H)])*((x1a - S)/S);
va = (vcterm/H)*(Exp[k1 + (k2/H)]*(y1a) + G*(1 - Exp[-g*((S - x1a)/S)]*(y1a/H));
duadx1 = D[ua, x1a];
dvady1 = D[va, y1a];
duady1 = D[ua, y1a];
dvadx1 = D[va, x1a];
x1a = u*d;
y1a = u*h - ((u*h)*(1 - u)^2) - (d*y3 - h)*(1 - u)*u^2;
x1apu = D[x1a, u];
y1apu = D[y1a, u];
y1ap = y1apu/x1apu;
ds1a = ((1 + y1ap^2)^0.5)*x1apu;
costh1a = x1apu/ds1a;
sinth1a = y1apu/ds1a;
gamma1asc = (duady1 + dvadx1)*((x1apu*y1apu)/(ds1a^2));
ethss1a = duadx1*(costh1a^2) + dvady1*(sinth1a^2) + gamma1asc;
Umem1underH = 0.5*Ewire*Ar*((ethss1a - Alphawire*dT)^2)*ds1a;

```

(* Umem1overH calculates the strain energy of wire represented by curve 1 in domain C due to stretch *)

```

Clear[x1c]
Clear[y1c]
uc1 = (ucterm/S)*(x1c) + A*(1 - Exp[-a*(y1c/H)])*((x1c - S)/S) - B*(1 - Exp[-b*((y1c - H)/H)]*(x1c/S));
vc1 = vcterm*(Exp[k1 + (k2/y1c)]) + G*(1 - Exp[-g*((S - x1c)/S)]*(H/y1c) + K*((y1c - H)/H)*(Exp[k1 + (k2/y1c)]));
ducdx1 = D[uc1, x1c];
dvcdy1 = D[vc1, y1c];
ducdy1 = D[uc1, y1c];
dvcdx1 = D[vc1, x1c];
x1c = u*d;
y1c = u*h - ((u*h)*(1 - u)^2) - (d*y3 - h)*(1 - u)*u^2;
x1cpu = D[x1c, u];
y1cpu = D[y1c, u];
y1cp = y1cpu/x1cpu;
ds1c = ((1 + y1cp^2)^0.5)*x1cpu;
costh1c = x1cpu/ds1c;
sinth1c = y1cpu/ds1c;
gamma1csc = (ducdy1 + dvcdx1)*((x1cpu*y1cpu)/(ds1c^2));
ethss1c = ducdx1*(costh1c^2) + dvcdy1*(sinth1c^2) + gamma1csc;
Umem1overH = 0.5*Ewire*Ar*((ethss1c - Alphawire*dT)^2)*ds1c;

```

(* Umem2overH calculates the strain energy of wire represented by curve 2 in domain C due to stretch *)

```

Clear[x2c]
Clear[y2c]
uc2 = (ucterm/S)*(x2c) + A*(1 - Exp[-a*(y2c/H)])*((x2c - S)/S) - B*(1 - Exp[-b*((y2c - H)/H)])*(x2c/S);
vc2 = vcterm*(Exp[k1 + (k2/y2c)]) + G*(1 - Exp[-g*((S - x2c)/S)])*(H/y2c) + K*((y2c - H)/H)*(Exp[k1 + (k2/y2c)]);
ducdx2 = D[uc2, x2c];
dvcdy2 = D[vc2, y2c];
ducdy2 = D[uc2, y2c];
dvcdx2 = D[vc2, x2c];
x2c = ((1 - v)*d) + (v*S) + ((S - d)*(1 - v)*v^2);
y2c = (1 - v)*h + (v*H) + (((S - d)*y3 - (H - h))*v*(1 - v^2 + v^2));
dy2 = D[y2c, v];
dx2 = D[x2c, v];
y2p = dy2/dx2;
ds2 = ((1 + y2p^2)^(0.5))*dx2;
costh2 = dx2/ds2;
sinth2 = dy2/ds2;
gamma2sc = (ducdy2 + dvcdx2)*((dx2*dy2)/(ds2^2));
ethss2 = ducdx2*(costh2^2) + dvcdy2*(sinth2^2) + gamma2sc;
Umem2overH = 0.5*Ewire*Ar*((ethss2 - Alphawire*dT)^2)*ds2;

```

(* UencapunderH calculates the strain energy in the encapsulant in domain A *)

```

Clear[x1a]
Clear[y1a]
ua = (ucterm/S)*(x1a) + A*(1 - Exp[-a*(y1a/H)])*((x1a - S)/S);
va = (vcterm/H)*(Exp[k1 + (k2/H)])*(y1a) + G*(1 - Exp[-g*((S - x1a)/S)])*(y1a/H);
duadx1 = D[ua, x1a];
dvady1 = D[va, y1a];
duady1 = D[ua, y1a];
dvadx1 = D[va, x1a];
efinal1 = duadx1 - (encapalpha*dT);
efinal2 = dvady1 - (encapalpha*dT);
efinal3 = duady1 + dvadx1;
inter1 = efinal1*SM[[1, 1]] + efinal2*SM[[2, 1]] + efinal3*SM[[3, 1]];
inter2 = efinal1*SM[[1, 2]] + efinal2*SM[[2, 2]] + efinal3*SM[[3, 2]];
inter3 = efinal1*SM[[1, 3]] + efinal2*SM[[2, 3]] + efinal3*SM[[3, 3]];
integrand = inter1*efinal1 + inter2*efinal2 + inter3*efinal3;
UencapunderH = (1/2)*integrand;

```

(* UencapoverH calculates the strain energy in the encapsulant in domain C *)

```

Clear[x1c]
Clear[y1c]
uc1 = (ucterm/S)*(x1c) + A*(1 - Exp[-a*(y1c/H)])*((x1c - S)/S) - B*(1 - Exp[-b*((y1c - H)/H)])*(x1c/S);

```

```

vc1 = vcterm*(Exp[k1 + (k2/y1c)]) + G*(1 - Exp[-g*((S - x1c)/S)])*(H/y1c) + K*((y1c -
H)/H)*(Exp[k1 + (k2/y1c)]);
ducdx1 = D[uc1, x1c];
dvcdy1 = D[vc1, y1c];
ducdy1 = D[uc1, y1c];
dvcdx1 = D[vc1, x1c];
efinal1 = ducdx1 - (encapalpha*dT);
efinal2 = dvcdy1 - (encapalpha*dT);
efinal3 = ducdy1 + dvcdx1;
inter1 = efinal1*SM[[1, 1]] + efinal2*SM[[2, 1]] + efinal3*SM[[3, 1]];
inter2 = efinal1*SM[[1, 2]] + efinal2*SM[[2, 2]] + efinal3*SM[[3, 2]];
inter3 = efinal1*SM[[1, 3]] + efinal2*SM[[2, 3]] + efinal3*SM[[3, 3]];
integrand = inter1*efinal1 + inter2*efinal2 + inter3*efinal3;
UencapoverH = (1/2)*integrand;

```

```

(* UencapoverDie calculates the strain energy in the encapsulant in domain B *)
ub = ucterm + (u2sub + udie)*((xx - S)/L) + B*(1 - Exp[-b*((yy - H)/H)])*((xx - (S +
L))/L);
vb = (vcterm + K*((yy - H)/H))*(Exp[k1*((S + L - xx)/L) + (k2/yy)]);
dubdx = D[ub, xx];
dvbdy = D[vb, yy];
dubdy = D[ub, yy];
dvbdx = D[vb, xx];
efinal1 = dubdx - (encapalpha*dT);
efinal2 = dvbdy - (encapalpha*dT);
efinal3 = dubdy + dvbdx;
inter1 = efinal1*SM[[1, 1]] + efinal2*SM[[2, 1]] + efinal3*SM[[3, 1]];
inter2 = efinal1*SM[[1, 2]] + efinal2*SM[[2, 2]] + efinal3*SM[[3, 2]];
inter3 = efinal1*SM[[1, 3]] + efinal2*SM[[2, 3]] + efinal3*SM[[3, 3]];
integrand = inter1*efinal1 + inter2*efinal2 + inter3*efinal3;
UencapoverDie = (1/2)*integrand;

```

```

(* U1sub calculates the strain energy in the substrate under the bond wire *)
U1sub = 0.5*Esub*(((u1sub/S) - subalpha*dT)^2)*subthick*S*planethk*(0.2);

```

```

(* U2sub calculates the strain energy in the substrate under the silicon die *)
U2sub = 0.5*Esub*(((u2sub/diespan) - subalpha*dT)^2)*subthick*diespan*planethk;

```

```

(* Udie_x calculates the strain energy in the die in x-direction*)
Udieinx = 0.5*Edie*(((udie/diespan) - diealpha*dT)^2)*(H - Hda)*diespan*planethk;

```

```

(* Udie_y calculates the strain energy in the die in y-direction *)
Udieiny = 0.5*Edie*(((vdie/(H - Hda)) - diealpha*dT)^2)*(H -
Hda)*diespan*planethk*(0.1);

```

```

(* Udieattach_xy calculates the strain energy in the die attach due to shear deformation *)

```

```
Udieattachinxy = 0.5*(Edieattach/(2*(1 + nudieattach)))*(((udie -
u2sub)/Hda)^2)*Hda*diespan*planethk*(0.1);
```

(* Udieattach_y calculates the strain energy in the die attach in y-direction *)

```
Udieattachiny = 0.5*Edieattach*(((vdieattach/Hda) -
daalpha*dT)^2)*Hda*diespan*planethk*(0.1);
```

```
expr1 = Uwire1underH + Umem1underH;
expr2 = Uwire1overH + Umem1overH;
expr3 = Uwire2overH + Umem2overH;
expr4 = UencapunderH*pitch;
expr5 = UencapoverH*pitch;
expr6 = UencapoverDie*pitch;
expr7 = U1sub + U2sub + Udieinx + Udieiny + Udieattachinxy + Udieattachiny;
r1 = { A, B, u1sub, u2sub, udie, vdie, vdieattach, K, G };
coeffm = { {1, 2, 3, 4, 5, 6, 7, 8, 9},
            {1, 2, 3, 4, 5, 6, 7, 8, 9},
            {1, 2, 3, 4, 5, 6, 7, 8, 9},
            {1, 2, 3, 4, 5, 6, 7, 8, 9},
            {1, 2, 3, 4, 5, 6, 7, 8, 9},
            {1, 2, 3, 4, 5, 6, 7, 8, 9},
            {1, 2, 3, 4, 5, 6, 7, 8, 9},
            {1, 2, 3, 4, 5, 6, 7, 8, 9},
            {1, 2, 3, 4, 5, 6, 7, 8, 9}
          };
```

```
For [ i = 1, i ≤ 9, ++i,
  For [ j = 1, j ≤ 9, ++j,
    coeffm[[i, j]] = NIntegrate[ Coefficient[ D[ expr1, r1[[i]] ], r1[[j]] ], {u, 0, t} ] +
                    NIntegrate[ Coefficient[ D[ expr2, r1[[i]] ], r1[[j]] ], {u, t, 1} ] +
                    NIntegrate[ Coefficient[ D[ expr3, r1[[i]] ], r1[[j]] ], {v, 0, 1} ] +
                    NIntegrate[ Coefficient[ D[ expr4, r1[[i]] ], r1[[j]] ], {y1a, 0, H},
                                {x1a, 0, S} ] +
                    NIntegrate[ Coefficient[ D[ expr5, r1[[i]] ], r1[[j]] ], {y1c, H,
                                Hc}, {x1c, 0, S} ] +
                    NIntegrate[ Coefficient[ D[ expr6, r1[[i]] ], r1[[j]] ], {yy, H, Hc},
                                {xx, S, Sc} ] +
                    Coefficient[ D[expr7, r1[[i]] ], r1[[j]] ]
  ]
]
```

```
constm = { 1, 2, 3, 4, 5, 6, 7, 8, 9};
```

```
For [ i = 1, i ≤ 9, ++i,
  pdexpr1 = D [ expr1, r1[[i]] ];
  pdexpr2 = D [ expr2, r1[[i]] ];
  pdexpr3 = D [ expr3, r1[[i]] ];
  pdexpr4 = D [ expr4, r1[[i]] ];
```

```

pdexpr5 = D [ expr5, r1[[i]] ];
pdexpr6 = D [ expr6, r1[[i]] ];
pdexpr7 = D [ expr7, r1[[i]] ];
{A, B, u1sub, u2sub, udie, vdie, vdieattach, K,
G} = {0.0, 0.0, 0.0, 0.0, 0.0, 0.0, 0.0, 0.0, 0.0};
constm[[i]] = -1*( NIntegrate[ Evaluate[ pdexpr1], {u, 0, t} ] +
NIntegrate[ Evaluate[ pdexpr2], {u, t, 1} ] +
NIntegrate[Evaluate[pdexpr3], {v, 0, 1} ] +
NIntegrate[Evaluate[pdexpr4], {y1a, 0, H}, {x1a, 0, S} ] +
NIntegrate[Evaluate[pdexpr5], {y1c, H, Hc}, {x1c, 0, S} ] +
NIntegrate[Evaluate[pdexpr6], {yy, H, Hc}, {xx, S, Sc} ] +
Evaluate[ pdexpr7 ] );
Clear[A, B, u1sub, u2sub, udie, vdie, vdieattach, K, G]
]
coeffm;
constm;
params = Inverse[ coeffm]. constm;

(* Calculating the total elastic strain in the wire *)
Clear[u]
Clear[v]
a1 = d*(S - d)/((2*S) + d);
b1 = 2*(H - h)/((S - d)^2);
c1 = 3*h/(d^2);
y3 = a1*(b1 + c1);
u = Table[i, {i, 0, 1, 0.0001}];
x1 = u*d;
y1 = u*h - ((u*h)*(1 - u)^2) - (d*y3 - h)*(1 - u)*u^2;
ymax = Max[y1];
For[z = 1, z ≤ 10001, z++, If[y1[[z]] ≤ H, t = (z)/10000]]
t;
Clear[u];
f2 = -2*10^(-11)*(Eencap^2) + 4*10^(-6)*Eencap + 0.168;
b = (-4*H/S)*Log[1 - f2];
f4 = -5*10^(-11)*(Eencap^2) + 3*10^(-6)*Eencap + 1.0081;
k1 = Log[f4];
a = 4.0449*(10^-009)*Eencap^2 + (-8.5807)*(10^-005)*Eencap + 3.3374;
g = 1.6309*(10^-009)*Eencap^2 + (-1.4923)*(10^-004)*Eencap + 6.4482;
k2 = 0.05;
A = params[[1]];
B = params[[2]];
u1sub = params[[3]];
u2sub = params[[4]];
udie = params[[5]];
vdie = params[[6]];
vdieattach = params[[7]];

```

```

K = params[[8]];
G = params[[9]];
ucterm = u1sub;
vcterm = vdie + vdieattach;
a1 = d*(S - d)/((2*S) + d);
b1 = 2*(H - h)/((S - d)^2);
c1 = 3*h/(d^2);
y3 = a1*(b1 + c1);
x1a = u*d;
y1a = u*h - ((u*h)*(1 - u)^2) - (d*y3 - h)*(1 - u)*u^2;
y1apu = D[y1a, u];
x1apu = D[x1a, u];
y1ap = y1apu/x1apu;
y1adp = D[y1ap, u]/x1apu;
cur1a = (y1adp)/((1 + (y1ap)^2)^1.5);          templ1a = cur1a;
x1c = u*d;
y1c = u*h - ((u*h)*(1 - u)^2) - (d*y3 - h)*(1 - u)*u^2;
y1cpu = D[y1c, u];
x1cpu = D[x1c, u];
y1cp = y1cpu/x1cpu;
y1cdp = D[y1cp, u]/x1cpu;
cur1c = (y1cdp)/((1 + (y1cp)^2)^1.5);          \
templ1c = cur1c;
x2c = ((1 - v)*d) + (v*S) + ((S - d)*(1 - v)*v^2);
y2c = (1 - v)*h + (v*H) + (((S - d)*y3 - (H - h))*v*(1 - v^2 + v^2));
y2cpv = D[y2c, v];
x2cpv = D[x2c, v];
y2cp = y2cpv/x2cpv;
y2cdp = D[y2cp, v]/x2cpv;
cur2c = (y2cdp)/((1 + (y2cp)^2)^1.5);          temp2c = cur2c;
Clear[x1a, x1c, x2c, y1a, y1c, y2c]
ua = (ucterm/S)*(x1a) + A*(1 - Exp[-a*(y1a/H)])*((x1a - S)/S);
va = (vcterm/H)*(Exp[k1 + (k2/H)]*(y1a) + G*(1 - Exp[-g*((S - x1a)/S)]*(y1a/H));
duadx1 = D[ua, x1a];
dvady1 = D[va, y1a];
duady1 = D[ua, y1a];
dvadx1 = D[va, x1a];
x1a = u*d;
y1a = u*h - ((u*h)*(1 - u)^2) - (d*y3 - h)*(1 - u)*u^2;
x1apu = D[x1a, u];
y1apu = D[y1a, u];
y1ap = y1apu/x1apu;
ds1a = ((1 + y1ap^2)^0.5)*x1apu;
costh1a = x1apu/ds1a;
sinth1a = y1apu/ds1a;
gamma1asc = (duady1 + dvadx1)*((x1apu*y1apu)/(ds1a^2));

```

$ethss1a = duadx1*(cosh1a^2) + dvady1*(sinh1a^2) + gamma1asc;$
 $x1af = x1a + ua;$
 $y1af = y1a + va;$
 $x1afpu = D[x1af, u];$
 $y1afpu = D[y1af, u];$
 $y1afpx1af = y1afpu/x1afpu;$
 $y1afdpu = D[y1afpu, u];$
 $x1afdpu = D[x1afpu, u];$
 $y1afdpx1af = (x1afpu*y1afdpu - y1afpu*x1afdpu)/((x1afpu)^3);$

$uc1 = (ucterm/S)*(x1c) + A*(1 - Exp[-a*(y1c/H)]*((x1c - S)/S) - B*(1 - Exp[-b*((y1c - H)/H)]*(x1c/S));$
 $vc1 = vcterm*(Exp[k1 + (k2/y1c)]) + G*(1 - Exp[-g*((S - x1c)/S)]*(H/y1c) + K*((y1c - H)/H)*(Exp[k1 + (k2/y1c)]);$
 $ducdx1 = D[uc1, x1c];$
 $dvcdy1 = D[vc1, y1c];$
 $ducdy1 = D[uc1, y1c];$
 $dvcdx1 = D[vc1, x1c];$
 $x1c = u*d;$
 $y1c = u*h - ((u*h)*(1 - u)^2) - (d*y3 - h)*(1 - u)*u^2;$
 $x1cpu = D[x1c, u];$
 $y1cpu = D[y1c, u];$
 $y1cp = y1cpu/x1cpu;$
 $costh1c = x1cpu/ds1c;$
 $sinth1c = y1cpu/ds1c;$
 $ds1c = ((1 + y1cp^2)^0.5)*x1cpu;$
 $gamma1csc = (ducdy1 + dvcdx1)*((x1cpu*y1cpu)/(ds1c^2));$
 $ethss1c = ducdx1*(cosh1c^2) + dvcdy1*(sinh1c^2) + gamma1csc;$
 $x1cf = x1c + uc1;$
 $y1cf = y1c + vc1;$
 $x1cfpu = D[x1cf, u];$
 $y1cfpu = D[y1cf, u];$
 $y1cfpx1cf = y1cfpu/x1cfpu;$
 $x1cfdpu = D[x1cfpu, u];$
 $y1cfdpu = D[y1cfpu, u];$
 $y1cfdpx1cf = (x1cfpu*y1cfdpu - y1cfpu*x1cfdpu)/((x1cfpu)^3);$

$uc2 = (ucterm/S)*(x2c) + A*(1 - Exp[-a*(y2c/H)]*((x2c - S)/S) - B*(1 - Exp[-b*((y2c - H)/H)]*(x2c/S));$
 $vc2 = vcterm*(Exp[k1 + (k2/y2c)]) + G*(1 - Exp[-g*((S - x2c)/S)]*(H/y2c) + K*((y2c - H)/H)*(Exp[k1 + (k2/y2c)]);$
 $ducdx2 = D[uc2, x2c];$
 $dvcdy2 = D[vc2, y2c];$
 $ducdy2 = D[uc2, y2c];$
 $dvcdx2 = D[vc2, x2c];$
 $x2c = ((1 - v)*d) + (v*S) + ((S - d)*(1 - v)*v^2);$

```

y2c = (1 - v)*h + (v*H) + (((S - d)*y3 - (H - h))*v*(1 - v^2 + v^2));
dy2 = D[y2c, v];
dx2 = D[x2c, v];
y2p = dy2/dx2;
ds2 = ((1 + y2p^2)^(0.5))*dx2;
costh2 = dx2/ds2;
sinh2 = dy2/ds2;
gamma2sc = (ducdy2 + dvcdx2)*((dx2*dy2)/(ds2^2));
ethss2 = ducdx2*(costh2^2) + dvcdy2*(sinh2^2) + gamma2sc;
x2cf = x2c + uc2;
y2cf = y2c + vc2;
x2cfpv = D[x2cf, v];
y2cfpv = D[y2cf, v];
y2cfpx2cf = y2cfpv/x2cfpv;
x2cfdpv = D[x2cfpv, v];
y2cfdpv = D[y2cfpv, v];
y2cfdpvx2cf = (x2cfpv*y2cfdpv - y2cfpv*x2cfdpv)/((x2cfpv)^3);

```

```

cur1af = y1afdpx1af/((1 + y1afpx1af^2)^1.5);
cur1cf = y1cfdpx1cf/((1 + y1cfpx1cf^2)^1.5);
cur2f = y2cfdpx2cf/((1 + y2cfpx2cf^2)^1.5);

```

```
Clear[u]
```

```

p11 = ParametricPlot[{x1a, ((cur1af - temp1a)*-dia/2)}, {u, 0, t}];
p12 = ParametricPlot[{x1c, ((cur1cf - temp1c)*-dia/2)}, {u, t, 1}];
p13 = ParametricPlot[{x2c, ((cur2f - temp2c)*-dia/2)}, {v, 0, 1}];
Show[{p11, p12, p13}]

```

```
Clear[u]
```

```

encapstrain1a = ethss1a + (Sign[ethss1a])*Abs[((cur1af - temp1a)*-dia/2)] -
Alphawire*dT;
encapstrain1c = ethss1c + (Sign[ethss1c])*Abs[((cur1cf - temp1c)*-dia/2)] -
Alphawire*dT;
encapstrain2 = ethss2 + (Sign[ethss2])*Abs[((cur2f - temp2c)*-dia/2)] - Alphawire*dT;
p1 = ParametricPlot[{x1a, encapstrain1a}, {u, 0, t}];
p2 = ParametricPlot[{x1c, encapstrain1c}, {u, t, 1}];
p3 = ParametricPlot[{x2c, encapstrain2}, {v, 0, 1}];
Show[{p1, p2, p3}]

```

```
xvalues = Table[i, {i, 0, S, (S/100)}];
```

```
Clear[u]
```

```
u = {};
```

```
vx2 = {};
```

```
For[j = 1, j ≤ Length[xvalues], ++j, temp = xvalues[[j]]; If[temp ≤ d, u = AppendTo[u, temp/d], vx2 = AppendTo[vx2, temp]] ]
```

```

u1a = {};
u1c = {};
For[j = 1, j ≤ Length[u], ++j, utemp = u[[j]]; ut = utemp; ya = ut*h - ((ut*h)*(1 - ut)^2) -
(d*y3 - h)*(1 - ut)*ut^2; If[ya ≤ h, u1a = AppendTo[u1a, u[[j]], u1c = AppendTo[u1c,
u[[j]] ] ]

v = {};
For[j = 1, j ≤ Length[vx2], ++j, temp = vx2[[j]]; vtemp = Solve[((1 - vv)*d) + (vv*S) +
((S - d)*(1 - vv)*vv^2) - vx2[[j]] == 0, vv]; vtemp = vv /. vtemp; Print["vtemp=",
vtemp];
For[jj = 1, jj ≤ Length[vtemp], ++jj, If[(vtemp[[jj]] > 0 && vtemp[[jj]] ≤ 1), (mm
= jj) && ( v = AppendTo[v, vtemp[[mm]]])] ]

Clear[u]
u = u1a;
axialf1a = Evaluate[ethss1a - (Alphawire*dT)];
bendf1a = Evaluate[((cur1af - temp1a)*-dia/2)];
totalstrn1a = Evaluate[axialf1a + (Sign[axialf1a])*Abs[((cur1af - temp1a)*(-dia/2))] ];

u = u1c;
axialf1c = Evaluate[ethss1c - (Alphawire*dT)];
bendf1c = Evaluate[((cur1cf - temp1c)*-dia/2)];
totalstrn1c = Evaluate[axialf1c + (Sign[axialf1c])*Abs[((cur1cf - temp1c)*(-dia/2))]];

v = v;
axialf2 = Evaluate[ethss2 - (Alphawire*dT)];
bendf2 = Evaluate[((cur2f - temp2c)*-dia/2)];
totalstrn2 = Evaluate[axialf2 + (Sign[axialf2])*Abs[((cur2f - temp2c)*(- dia/2))]];

totalstrain = totalstrn1a;
For[ j = 1, j ≤ Length[totalstrn1c], ++j, totalstrain = AppendTo[totalstrain,
totalstrn1c[[j]] ] ]
For[ j = 1, j ≤ Length[totalstrn2], ++j, totalstrain = AppendTo[totalstrain,
totalstrn2[[j]]]]

modelgraph = {};
For[j = 1, j ≤ Length[totalstrain], ++j, temp = {xvalues[[j]], totalstrain[[j]]}; modelgraph
= AppendTo[modelgraph, temp]]
p21 = ListPlot[modelgraph, PlotJoined -> True]

axialfinal = axialf1a;
For[ j = 1, j ≤ Length[axialf1c], ++j, axialfinal = AppendTo[axialfinal, axialf1c[[j]] ] ]
For[ j = 1, j ≤ Length[axialf2], ++j, axialfinal = AppendTo[axialfinal, axialf2[[j]] ] ]
axialfinal

bendfinal = bendf1a;

```

```
For[ j = 1,  
j ≤ Length[bendf1c], ++j, bendfinal = AppendTo[bendfinal, bendf1c[[j]]] ]  
For[ j = 1, j ≤ Length[bendf2], ++j, bendfinal = AppendTo[bendfinal, bendf2[[j]]] ]  
bendfinal
```

```
Print["Axial Strain at Ball bond=", axialfinal[[100]]]  
Print["Bend. Strain at Ball bond=", bendfinal[[100]]]  
Print["Total Strain at Ball bond=", totalstrain[[100]]]
```

References

- APL, "Physics-of-Failure (PoF) Reliability Assessment of Electronics for Mars Mission, NASA/JPL Contract #1243213 Mars Technology Program", August 2005.
- Carl de Boor, "A Practical Guide to Splines", Applied Mathematical Sciences, vol. 27, Springer-Verlag, New York, pp. 66-67, 1978.
- Chandrasekaran, A., "Effect of mold compound on Au-Al wirebond-bond pad intermetallic formation", Masters Thesis 2004, University of Maryland-College Park
- Chidambaram, N. V., "A Numerical and Experimental Study of Temperature Cycle Wire Bond Failure", Proceeding of the 41st Electronic Components and Technology Conference, pp. 877-882, May 1991.
- Chylak, B., Lee, L., Babinetz, S., Kwon, O. D., "Advanced Ultra-Low-Loop Wire Bonds", SEMICON China, 2006.
- Dasgupta, A., "Characterization of Anisotropic Conductive Adhesive", CALCE Consortium Report, Project No. C02-31, 2002.
- Dasgupta, A., Pecht, M., "Material failure mechanisms and damage models", IEEE Transactions on Reliability, Volume 40, Issue 5, pp: 531 – 536, , Dec. 1991
- Groover, R., Shu, W. K., Lee, S. S., "Wire Bond Loop Profile Development for Fine Pitch-Long wire Assembly", IEEE Transactions on Semiconductor Manufacturing, vol. 7, no. 3, pp. 393-399, Aug 1994.
- Harman, G., "Wire Bonding in Microelectronics Materials, Processes, Reliability and Yield", Second Edition, McGraw Hill, 1997.
- Harman, G., "Wire bonding in microelectronics", Second Edition, 1997, McGraw –Hill, New York, pp. 232-235.
- Harman, G. G., "Metallurgical Failure Modes of Wirebonds", Proceedings of the 12th Annual International Reliability Physics Symposium, p131-141, 1974.
- Hu, J. M., Pecht, M., and Dasgupta, A., "A probabilistic approach for predicting thermal fatigue life of wire bonding in microelectronics", Journal of Electronic Packaging, Vol. 113, pp 275-285, 1991.
- Kulicke & Soffa, "AW-29 Gold Bonding Wire for Universal Use in Discrete and IC (Large Dia) Applications", www.kns.com, Product Literature, 2001.
- Meyyappan, K., P., McCluskey, P., Hansen, "Wire Fatigue Model For Power Electronic Modules", Proceedings of, IMECE'03, Washington, D. C., Nov 2003.
- Meyyappan, K., "Failure Prediction of Wire Bonds Due to Flexure", Ph. D. Dissertation 2004, University of Maryland-College Park.

Pang, H. L. J., Tan, T. L., Leonard, J. F., Chan, Y. S., "Reliability Assessment of a Wirebond Chip-on-Board Package Subjected to Accelerated Thermal Cycling Loading", IEEE/CPMT Electronic Packaging Technology Conference, pp. 93-97, 1997.

Pecht, M., "Handbook of Electronic Packaging", Marcel Dekker Inc., 1991

Pecht, M. G., Agarwal, R., McCluskey, P., Dishongh, T. Javadpour, S., Mahajan, R., "Electronic Packaging: Materials and Their Properties", CRC Press LLC, Washington, DC, 1999.

Pecht, M., Luu T. Nguyen, Edward B. Hakim , "Plastic Encapsulated Microelectronics", John Wiley & Sons, New York, NY, 1994.

Ramminger, S., Wachutka, G., "Wire Bond Failures in Power Modules", Proceedings of the IMECE'03, Washington DC, Nov 15-21, 2003.